



Naturalis Repository

Multi-stage metamorphism recorded in crustal xenoliths from Permian dykes of the region of Mrirt (Moroccan Central Massif)

Stéphanie Duchene, Jean-Luc Severac, Nadège Samalens, Youssef Driouch, Ahmed Ntarmouchant, Leo Kriegsman, Mohamed Dahire, Pierre Debat, Sophie Gouy

DOI:

<https://doi.org/10.1016/j.jafrearsci.2022.104636>

Downloaded from

[Naturalis Repository](#)

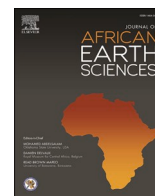
Article 25fa Dutch Copyright Act (DCA) - End User Rights

This publication is distributed under the terms of Article 25fa of the Dutch Copyright Act (Auteurswet) with consent from the author. Dutch law entitles the maker of a short scientific work funded either wholly or partially by Dutch public funds to make that work publicly available following a reasonable period after the work was first published, provided that reference is made to the source of the first publication of the work.

This publication is distributed under the Naturalis Biodiversity Center 'Taverne implementation' programme. In this programme, research output of Naturalis researchers and collection managers that complies with the legal requirements of Article 25fa of the Dutch Copyright Act is distributed online and free of barriers in the Naturalis institutional repository. Research output is distributed six months after its first online publication in the original published version and with proper attribution to the source of the original publication.

You are permitted to download and use the publication for personal purposes. All rights remain with the author(s) and copyrights owner(s) of this work. Any use of the publication other than authorized under this license or copyright law is prohibited.

If you believe that digital publication of certain material infringes any of your rights or (privacy) interests, please let the department of Collection Information know, stating your reasons. In case of a legitimate complaint, Collection Information will make the material inaccessible. Please contact us through email: collectie.informatie@naturalis.nl. We will contact you as soon as possible.



Multi-stage metamorphism recorded in crustal xenoliths from Permian dykes of the region of Mrirt (Moroccan Central Massif)

Stéphanie Duchene^{a,*}, Jean-Luc Severac^a, Nadège Samalens^a, Youssef Driouch^b, Ahmed Ntarmouchant^b, Leo Kriegsmann^c, Mohamed Dahire^b, Pierre Debat^a, Sophie Gouy^a

^a Université de Toulouse, GET, UMR 5563, OMP, CNRS, IRD, 14, avenue Edouard Belin, 31400, Toulouse, France

^b Département de Géologie, Laboratoire GERA, Université Mohamed Ben Abdellah, Faculté des Sciences Dhar El Mahraz, B.P. 1796, Fès-Atlas, Fès, Morocco

^c Naturalis Biodiversity Center, Research & Education Division, Dept. T&S, Darwinweg 2, NL-2333 CR, Leiden, Netherlands

ARTICLE INFO

Keywords:

Crustal xenoliths
Moroccan Central Massif
Metamorphism
Thermal history
Thermodynamic modelling
Magma-xenolith interactions

ABSTRACT

The Permian magmatic rocks from Morocco contain crustal xenoliths that sample the Variscan crust in a context of widespread magmatism. A series of such xenoliths was collected in Permian dykes of the Central Massif, in the region of Mrirt. The metapelitic xenoliths are silica poor to intermediate ($44 < \text{SiO}_2 < 57$ wt%) and alumina-rich ($17 < \text{Al}_2\text{O}_3 < 34$ wt%) and are notably enriched in some HFSE (Nb, Ta, Ti) and some transition elements (Cr, V, W, Ni). Their petrographic evolution depicts a multi-stage evolution from an early, subsolidus, metamorphic history related to regional metamorphism, of which biotite, garnet and sillimanite are the witnesses toward a late thermal evolution coeval with the entrapment in the magma, marked by pervasive partial melting and development of peritectic spinel and cordierite together with K-feldspar and ilmenite. The overall presence of corundum, which relates to the high Al_2O_3 content, accounts for an initial stage of partial melting and magma escape, prior to the entrapment in the magma. Textural and chemical observation suggests further xenolith digestion and melt flux from the xenoliths toward the magma during ascent. Thermodynamic modelling allowing the determination of the pressure-temperature history of each xenolith shows that the initial pressure varies from ca. 1.5 to ca. 6 kbar, which, considering lithostatic pressure, corresponds to sampling depths of ca. 5–25 km. The temperatures recorded by the parageneses coeval with partial melting in the presence of spinel are in the range 800–900 °C whatever the pressure, which accounts for rapid heating due to thermal equilibration with the magma. U–Th/Pb dating of monazite by EMPA gives a poorly resolved Permian age of 293 ± 25 Ma for metamorphism in the xenoliths, in accordance with the stratigraphic age of the host rock. The pressure conditions are similar to those recorded for regional metamorphism in the other Variscan outcrops in Morocco, namely the Jebilet, the Rehamna and the Aouli-Mibladen granitic complex, while the maximal temperatures are much higher. The xenoliths thus appear as typical of the Late Variscan geological evolution of the deep crust in the Moroccan Mesetas, where abundant magmatism was responsible for local crustal heating of a crust previously affected by regional metamorphism.

1. Introduction

The presence of granulite facies rocks and migmatites in metamorphic rocks formed at middle to lower crustal level in mountain belts accounts for high geothermal gradients ($>30^\circ/\text{km}$). Such gradients cannot be sustained by normal radioactivity in a crust of standard thickness. Their occurrence claims either for an increase of crustal thickness (England and Thompson, 1984), which induces an increase in radioactive heat production, or for additional heat sources associated to

orogenic processes. Specifically, the injection in the crust of magmas of mantle origin may explain significant increase of the temperature (e.g. Juez-Larré and Ter Voorde, 2009) whereas magma transfer ensures near-isothermal conditions in middle-low crustal level and high gradients at upper crustal levels (Depine et al., 2008). Magmatic and metamorphic rocks that outcrop together in high temperature orogenic crust are invaluable witnesses of crustal heating but prograde metamorphism is often obliterated by later retrogression associated to a long exhumation history in a thermally unstable orogenic crust. By contrast, crustal

* Corresponding author.

E-mail address: stephanie.duchene@get.omp.eu (S. Duchene).

<https://doi.org/10.1016/j.jafrearsci.2022.104636>

Received 23 August 2021; Received in revised form 13 June 2022; Accepted 17 June 2022

Available online 21 June 2022

1464-343X/© 2022 Elsevier Ltd. All rights reserved.

xenoliths transported to the surface in volcanic rocks have been shown to record the pressure-temperature conditions prevailing in the crust in the very moment of sampling by the magmas, thanks to their rapid ascent toward the surface. A remarkable example is that of the metamorphic xenoliths trapped in Neogene lavas of SE Spain (e.g. Cesare, 2000; Acosta-Vigil et al., 2010; Álvarez-Valero and Kriegsman, 2007),

that record, from west to east, both crustal thinning (decreasing pressure) and crustal heating (increasing temperature) and image crustal extension and increasing heat flux related to the opening of the Alborán Sea. Nevertheless, xenoliths also undergo strong albeit short heating during their ascent (Álvarez-Valero et al., 2015), possible partial melting and digestion, that may hamper the record of the PT conditions

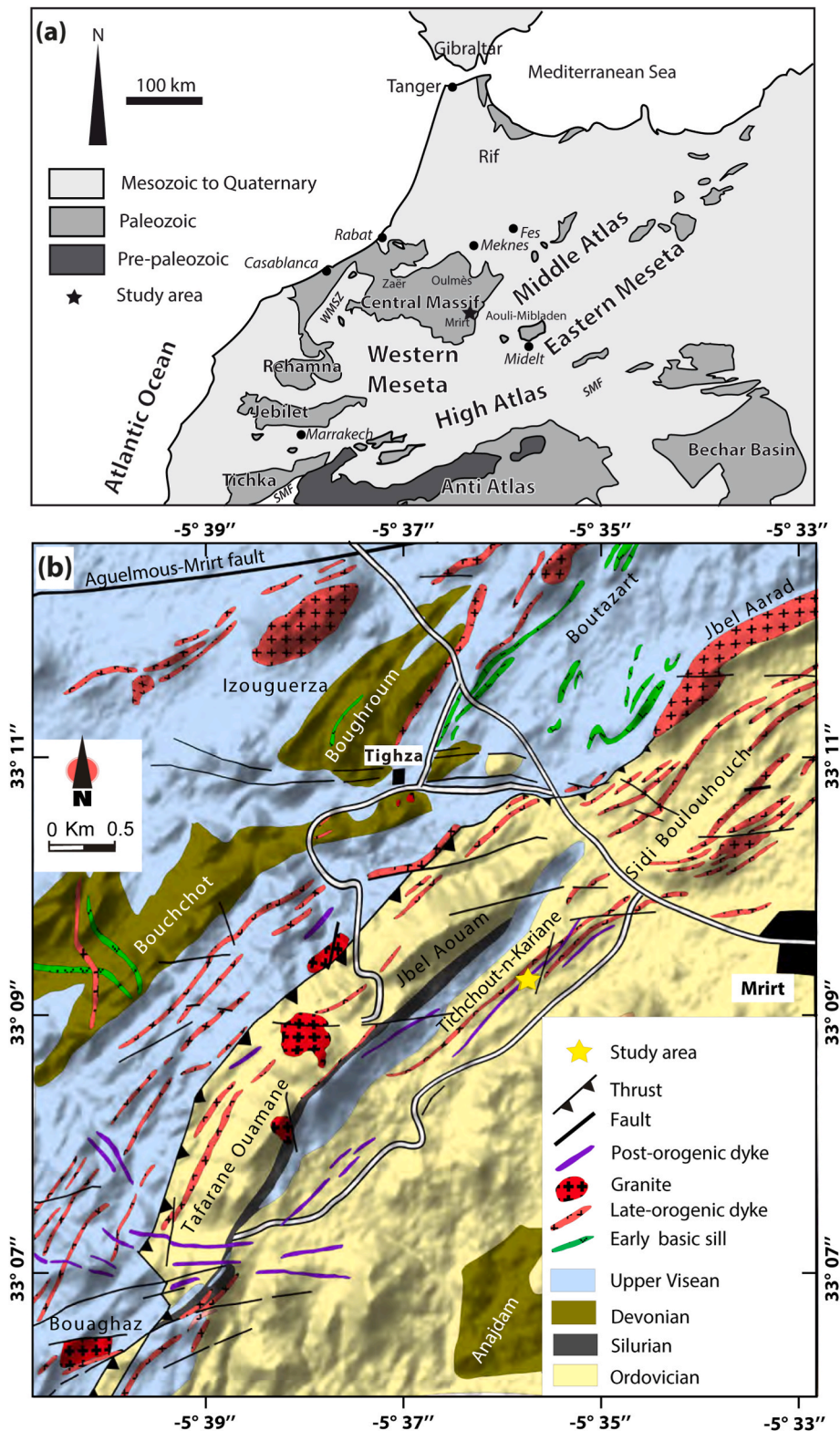


Fig. 1. Geological maps (a) Tectonic map of Morocco and location of the study area (b) Geological map of the study area (after Ntarmouchant, 2003).

prevailing during magma injection in the crust (e.g. Díaz-Alvarado et al. 2011; Johnson et al., 2011).

The Variscan crust underwent high-temperature, granulite facies metamorphism associated to magmatism in the Ivrea zone in the Alps (Kunz et al., 2018; Petri et al., 2017), Calabria (Graessner and Schenk, 2001; Fornelli et al., 2011; Duchene et al., 2013), Corsica (Corsini and Rolland, 2009; Rossi et al., 2015) and Pyrenees (Guitard et al., 1995; Siron et al., 2020). In Morocco, there are only limited outcrops of the Variscan median crust, that mainly shows MP/MT greenschist to amphibolite facies metamorphism. However, high temperature granulitic conditions are retrieved from abundant crustal xenoliths sampled both by Permian and Neogene magmatic rocks (Bouloton et al., 1991; Bouloton and Gasquet, 1995; Moukadiri and Bouloton, 1998; Ntarmouchant, 2003; Dostal et al., 2005; Elabouyi et al., 2019) that appear as a window into the underlying crust. Here we propose to study a set of crustal metapelitic xenoliths trapped in Permian dykes from the Moroccan Central Massif, in the late stages of the Variscan orogeny, in order to decipher the relative contributions to the metamorphic record of i) general metamorphism and ii) heating during magma emplacement. More specifically, through petrographic observation and thermodynamic modelling, we intend to retrieve the petrogenetic evolution of xenoliths, their pressure – temperature evolution from regional metamorphism toward entrapment in the magma during its ascent and explore the intensity of thermal and chemical crustal – melt interaction.

2. Geological context

In Morocco, witnesses of the Variscan belt are exposed in the Mauritaniides, in the Anti-Atlas and in the Meseta domain (Fig. 1a) as summarized by Simancas et al. (2005, 2009), Hoepffner et al. (2005) and Michard et al. (2008, 2010). It is believed that these domains represent the former Gondwana passive margin and are the southern termination of the Variscan belt (Simancas et al., 2005, 2009; Michard et al., 2010; Martínez Catalán et al., 2021). This passive margin was involved into the orogeny when closure of the Rheic ocean eventually led to the collision between Armorica and Gondwana. No remnant of an oceanic suture exists in the Moroccan Variscan belt, so that several models for the orogeny have been proposed, from that of an intra-continental orogeny (Piqué and Michard, 1989) to a subduction-related orogeny due to either south-eastward subduction of the Rheic ocean under the northern margin of Gondwana (Michard et al., 2010) or north-westward subduction of an eastern Paleotethyan oceanic domain (Roddaz et al., 2002; Stampfli and Borel, 2002) or a succession of both (Martínez Catalán et al., 2021).

The Central Massif is one of the Paleozoic massifs that constitute the Western Meseta domain, west of the Middle Atlas high. It is composed of a sequence from Cambrian to Permian sediments. The study area is located close to the locality of Mrirt (Fig. 1b), close to the Tighza Massif and is described in detail in Ntarmouchant (2003). The oldest Paleozoic, undifferentiated Cambrian-Ordovician sediments are detrital sandstones and pelites. Silurian sediments are black to purple shales which represent the decollement level for a series of Devonian-Carboniferous duplex system (Ben Abbou et al., 2001). The overlying Devonian sediments are intercalations of carbonates and pelites. The detrital Visean-Namurian stratas, progressively turning into continental deposits, are discordant on the Ordovician to Devonian sediments and have been interpreted as syn-tectonic sediments (Ben Abbou et al., 2001; Roddaz et al., 2002; Accotto et al., 2020) deposited in a foreland basin. Finally, the Hercynian structures are sealed by Upper Stephanian-Autunian continental redbeds that unconformably overlay the Visean-Namurian sediments and are affected by late Hercynian faulting.

Numerous gabbroic and doleritic bodies intrude the Carboniferous sedimentary layers and form vein swarms parallel to the Hercynian structures. Since they are folded together with the Carboniferous sediments, they are considered as late-Visean to Serpukovian in age (Ntarmouchant, 2003). Later magmatism takes the form of microgranitic

dykes or granitoid plutons that crosscut the Carboniferous stratas and structures, but are mainly oriented parallel to the schistosity. A final pulse of magmatic activity is represented by microgranodioritic enclave-rich dykes that crosscut the regional schistosity and all granitic bodies. As they do not cross the mesozoic stratas, those dykes are considered as Permo-Triassic in age.

The following chronology of magmatic events can be depicted in the Western Meseta domain. 1) The early magmatic stage, characterized by a bimodal association, is constrained at 358-330 Ma by U–Pb zircon dating in the Jebilet Massif (358-336 Ma, Delchini et al., 2018; 331.18–329.67 Ma, Essaifi et al., 2003). 2) The emplacement of syn-tectonic granodioritic to granitic bodies is dated by SHRIMP U–Pb dating on magmatic zircons from xenoliths by Dostal et al. (2005) at 328–285 Ma and by $^{40}\text{Ar}/^{39}\text{Ar}$ ages on a syn-tectonic granite and associated contact metamorphism between 280 and 295 Ma. These ages confirm earlier whole-rock Rb/Sr ages by Mrini et al. (1992) in the Jebilet massif and in the Oulmès and Ment area in the Central Massif. In the Tichka area, the granitic stocks have been dated by U–Pb on zircon at 295-280 Ma (Rossi et al., 2016). 3) Late to post-tectonic magmatism is generally considered as Permo-Triassic, based on whole-rock Rb–Sr data at 268 ± 6 Ma obtained on the Rehamna by Mrini et al. (1992) and white micas $^{40}\text{Ar}/^{39}\text{Ar}$ cooling ages (275 Ma) on a post-tectonic pluton from the Rehamna by Chopin et al. (2014), whereas U–Pb lower intercept age on a zircon rim from granulitic xenolith obtained by Dostal et al. (2005) suggests Jurassic activity at 235 ± 8 Ma. 4) In the Mrit area, a K–Ar age of 286 Ma obtained on a granitic dyke crosscut by microgranodioritic dyke (Cheilletz, 1984) provides an upper age limit, whereas the age for the latest dykes is constrained by Th/Pb on monazite in the associated Pb–Zn–Ag veins located 2 km south of the sampling area at 254 ± 16 Ma (Rossi et al., 2016).

The Paleozoic series of the Moroccan Variscan belt have been metamorphosed under greenschist to amphibolite facies conditions (Michard et al., 2008, 2010). The highest metamorphic conditions are observed along a NE-SW shear zone (the Western Meseta Shear Zone) that crosscut the Central, the Rehamna and the Jebilet massifs (Michard et al., 2008). The syn-tectonic metamorphic PT conditions in the Rehamna domain, reaching locally 620 °C, 6 kbar (Wernert et al., 2016), correspond to a MP/MT gradient of ca. 35 °C/km (Aghzer and Arenas, 1995, 1998). Similar temperatures (628 ± 50 °C) are recorded in the Jebilet area (Delchini et al., 2016). In the study area however, metamorphic conditions do not exceed greenschist facies conditions (365 ± 7 °C, Lahfid et al., 2019). The age for MP-MT metamorphism is constrained by few direct radiometric in the Rehamna by U–Pb dating on monazite and $^{40}\text{Ar}/^{39}\text{Ar}$ dating on amphibole and micas (Chopin et al., 2014; Wernert et al., 2016). The microstructural analysis associated to *in situ* dating depicts a multistage metamorphic history, beginning in the late Carboniferous (minimum $^{40}\text{Ar}/^{39}\text{Ar}$ age of ca. 310 Ma) with a prograde metamorphic phase associated to thickening followed by a syn-convergence exhumation phase at 310-295 Ma and ending in the Permian (292-275 Ma), while late tectonic granites were emplaced. Contact metamorphism related to syn-to post-tectonic magmatism is described in the Rehamna (Michard et al., 2010) and in the Jebilet (Delchini et al., 2016), where maximum temperature reaches 600 °C for maximal pressure of 3 kbar. In the Central Massif, metamorphic aureoles characterized by the presence of andalusite – biotite – K-feldspar association have been described around the syn-tectonic calc-alkaline plutons and the post-tectonic leucogranitic bodies in Zaër, Oulmès and Ment (Boushaba and Cailleux, 1992; Dahmani, 1995), which leads to pressure estimates of 1.3–2 kbar and maximal temperatures of 600 °C.

Moreover, metamorphic xenoliths of sedimentary origin and of high metamorphic grade (amphibolite to granulite facies conditions) have been sampled by late-to post-Hercynian magmatic bodies. In the Jebilet massif, late-hercynian granodioritic dykes contain both partially molten quartz, feldspar, biotite bearing gneisses and K-feldspar, plagioclase, cordierite, garnet, spinel, aluminosilicate, corundum and ilmenite bearing peraluminous enclaves (Bouloton et al., 1991; Bouloton and

Gasquet, 1995). In the quaternary basalts of the Middle Atlas, meta-sedimentary enclaves are characterized by a quartz-feldspar-sillimanite-garnet association, the rarity of biotite and the development of hercynite and orthopyroxene as a product of incongruent melting in the granulite facies (Moukadiri and Bouloton, 1998; van Hoeflaken, 2011). In the Zaër granitic pluton (a late-hercynian intrusion of the Central Massif), Haïmeur et al. (2003) describe a diversity of metapelitic enclaves, generally characterized by the presence of quartz, biotite, feldspar and cordierite. Several types of xenoliths are distinguished based on the presence or absence of aluminosilicate (andalusite partly replaced by fibrous sillimanite) and of corundum, pyroxene and spinel relics. Corresponding *PT* conditions vary from 600 to 650 °C, 2–2.5 kbar for andalusite bearing samples and 690–770 °C, 4–5 kbar in the spinel bearing xenoliths from the Zaër pluton (Haïmeur et al., 2003), 750–800 °C, 3.5–3.9 kbar in the Jebilet (Bouloton et al., 1991) and up to 900 °C, 9–11 kbar in the recent lavas from Middle Atlas (Moukadiri and Bouloton, 1998). Note also that granulite facies conditions (830–870 °C; 6 kbar) are reported for high-grade migmatites and enclaves associated to mafic to acidic magmatism from the Eastern Meseta domain (Elabouyi et al., 2019).

A set of crustal xenoliths has been collected in the locality of Kariane, 2 km east of Mrirt. Two dykes of 1–2 m in thickness intrude the Ordovician metasediments, with a broadly N40 orientation (Ntarmouchant, 2003) and can be followed over a distance of ca. 2 km (Fig. 2a). The emplacement depth of these dykes is not constrained. However, dykes of similar petrographic type and stratigraphic age have been shown to crosscut both Variscan plutons and the Paleozoic metasediments in the eastern Moroccan Massif Central (Ntarmouchant, 2003), or the contact metamorphic aureoles in the Tighza district (Rossi et al., 2016) and Oulmès and Ment plutons, for which pressures were estimated at 2 and 1.3 kbar respectively (Dahmani, 1995; Delchini et al., 2016), which converts to depths of 5–7.5 km (considering lithostatic pressure and a density of 2700 kg/m³). Moreover, metamorphic temperatures of the Paleozoic metasediments and the geothermal gradient prevailing during the Variscan collision have been estimated from RSCM in the Zaian mountains, and indicate depth of burial of 5–8.5 km (Lahfid et al.,

2019). We consider this as an upper limit for the emplacement depth of the dykes. One of the two dykes of the Kariane locality is of granitic composition and comprises few metasedimentary xenoliths. Only one of those xenoliths has been collected for this study (2Kar8). The second dyke is a microgranodioritic dyke which crosscuts the former one and is considered as post-orogenic since it also crosscuts the regional schistosity (Fig. 2b). It comprises numerous granitic and metasedimentary enclaves (metagreywackes and metapelites) (Ntarmouchant, 2003). The metasedimentary enclaves (Fig. 2c and d) are of small size (less than 10 cm), often elongated in shape and are non-oriented with respect to the dyke orientation. They can present or not an internal schistosity and also present a mineralogical variability (e.g. presence or not of andalusite). Twenty-one samples of metapelitic xenoliths from the microgranodioritic dyke have been collected at different places along the dyke and studied in thin sections. A representative set of those samples will be described in the following.

3. Methods

Samples collected in the field are centimeter size xenoliths (4–10 cm in length) included in their microgranodioritic or microgranitic host rock. Each sample has been prepared in order to separate i) one slice for thin section across the xenolith ii) one fragment (10–50 g) of xenolith for whole-rock analysis and iii) in eight samples, one fragment of the host rock (ca. 100 g) for whole-rock analysis. Thin sections have been made in the Géosciences environnement Toulouse laboratory (Toulouse, France). Samples selected for whole-rock analyses were crushed with a jaw crusher and pulverized in an agate mill. Five samples have been selected for detailed petrological investigation on the basis of petrographical observation by optical microscopy and SEM.

Petrological studies by SEM and EPMA were carried out at the Géosciences environnement Toulouse laboratory (GET, Université de Toulouse, France). Backscattered electron images as well as EDS maps were obtained using the JEOL JSM 6360 LV Scanning Electron Microscope (SEM) coupled to an energy dispersive spectrometry (EDS) analysis system Bruker Quantax 800 at the GET laboratory. The analytical

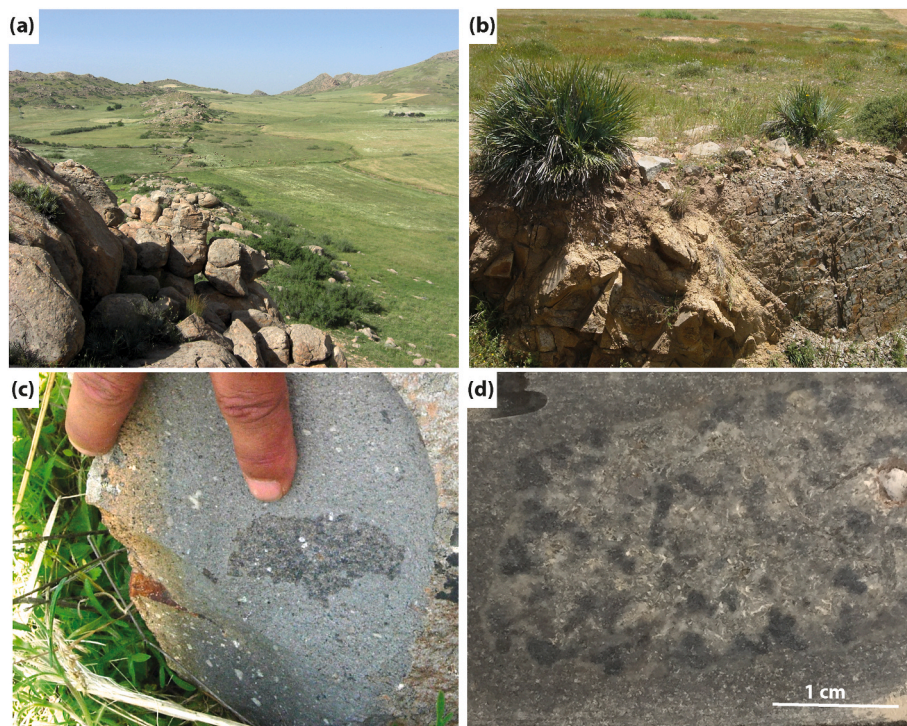


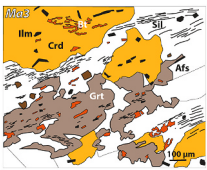
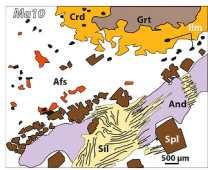
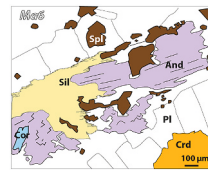
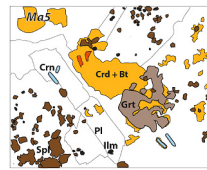
Fig. 2. Field photographs of the sampling area (Kariane locality) (a) Field view of the microgranodioritic dyke (b) Contact between the dyke and the Ordovician metasediments (c, d) Two examples of crustal xenoliths in the microgranodioritic host rock.

conditions used were 20 kV for the acceleration voltage, while a tungsten filament was used as the electron source. Semi-quantitative analytical composition were extracted from selected micro-domains in the chemical maps using the Bruker Hypermap software. Electron Probe Micro Analyses (EPMA) were obtained using the CAMECA SX 50 on polished thin sections using a beam current of 20 nA and an acceleration voltage of 15 keV for major elements. Monazites were analyzed for U–Th–Pb dating with an accelerating voltage of 15 kV and 300 nA probe current. The age and associated confidence interval were calculated with the Rpackage NileDam (Montel et al. 1996; Seydoux-Guillaume et al., 2012; Villa-Vialaneix et al., 2013). Analysis of the reference crystal MOACYR gave ages of 487 ± 25 Ma, in accordance with the recommended value of 474 ± 1 Ma (Seydoux-Guillaume et al., 2002), later revised to 504.3 ± 0.2 Ma (Gasquet et al. 2010) and 507.7 ± 1.3 Ma (Gonçalves et al., 2016).

Major elements and trace elements bulk-rock analyses were obtained by ICP-OES and ICP-MS respectively in the Service d'Analyse des Roches et des Minéraux (SARM), Nancy (France), following the analytical procedures described by Carignan et al. (2001).

Isochemical phase diagrams (pseudosections) were calculated in order to constrain metamorphic conditions, *i.e.* pressure and temperature range, of the aluminous xenoliths. Mineral equilibrium calculations were made in the NCKFMASHMT (Na₂O–CaO–K₂O–FeO–MgO–Al₂O₃–SiO₂–H₂O–MnO–TiO₂) system using Perple_X 07 software (Connolly, 2005, 2009) with the Holland and Powell (1998) database updated in 2002. Except for sample *Ma10*, the composition of the system was fixed at a local scale from SEM EDS maps. One pseudosection at the whole-rock scale has been calculated for sample *Ma10*. We have estimated the water content from $T-X_{H_2O}$ diagrams by choosing X_{H_2O} leading to the best agreement with observed assemblages as described in the petrography section, in particular the low volume of hydrous phases (namely biotite and cordierite). The solid solutions models are: biotite (Tajčmanová et al., 2009); chlorite (Holland and Powell, 1998); garnet (Holland and Powell, 1998); melt (Holland and Powell, 1998; White et al., 2001); cordierite (Berman and Aranovitch, 1996); plagioclase (Newton et al., 1980); K-feldspar (Waldbaum and Thompson, 1968); ilmenite (White et al., 2000); spinel (Holland and Powell, 1998); staurolite (Holland and Powell, 1998) and white mica (Coggon and Holland, 2002). Phase abbreviations are from Whitney and Evans (2010).

Table 1
Summary of petrological description of xenoliths.

	Ma3	Ma10	Ma6 and Kar2b	Ma 5
				
Xenolith chemistry	SiO ₂ 46.76% Al ₂ O ₃ 20.26% ΣREE 1317 ppm	SiO ₂ 44.07% Al ₂ O ₃ 33.84% ΣREE 1297 ppm	SiO ₂ 56.24% (<i>Ma6</i>) 44.99% (<i>Kar2b</i>) Al ₂ O ₃ 24.91% (<i>Ma6</i>) 30.99% (<i>Kar2b</i>) ΣREE 522 ppm (<i>Ma6</i>) 873 ppm (<i>Kar2b</i>)	SiO ₂ 44.99% Al ₂ O ₃ 30.99% ΣREE 1495 ppm
Pre-entrapment metamorphism remnants	Biotite, sillimanite, garnet	Andalusite, garnet	Andalusite, corundum	Garnet, corundum, biotite, ilmenite
Contact metamorphism	Garnet, spinel, alkali feldspar, biotite, ilmenite, melt Late cordierite, K-feldspar	Plagioclase, alkali feldspar, biotite, spinel, ilmenite, sillimanite, cordierite, melt	Spinel, plagioclase, biotite, sillimanite, cordierite, melt	Spinel, cordierite, corundum, ilmenite, plagioclase, Afs, melt
Mineral chemistry	Afs Or 62–90 Spl X_{Fe} 0.67–0.72 Grt X_{Alm} 0.64–0.73 Bt X_{Mg} 0.45 TiO ₂ 6–8%	Pl An 35–45 Afs Or 47–92 Spl X_{Fe} 0.63–0.79 Grt X_{Alm} 0.59–0.67 Bt X_{Mg} 0.4–0.56 TiO ₂ 3–7%	Pl An26–74 (<i>Ma6</i>) An15–45 (<i>Kar2b</i>) Afs Or 57–88 Spl X_{Fe} 0.64–0.69 (<i>Ma6</i>) X_{Fe} 0.70–0.74 (<i>Kar2b</i>)	Pl An 45–53 Spl X_{Fe} 0.57–0.64 Bt X_{Mg} 0.49–0.56 TiO ₂ < 5%
Contact <i>P-T</i> conditions	$P > 5$ kbar T 850–900 °C	P 4–6 kbar T 850 °C	$P < 2$ kbar $T > 900$ °C	$P < 5$ kbar T 800–850 °C

4. Petrography

4.1. Xenolith *Ma3*

Sample *Ma3* (Table 1) is characterized by a foliation underlined by biotite, sillimanite and elongated garnet (Fig. 3a and b, Fig. 4a). Crystals of biotite are sometimes skeletal (Figs. 3a and 4a). Garnet forms elongated corroded crystals included in alkali-feldspar and contains inclusions of ilmenite, biotite and numerous sillimanite needles oriented parallel to the main foliation (Figs. 3a and 4a). Spinel is rimmed by alkali-feldspar and often contains an inner foliation parallel to the main foliation (Fig. 3b). Cordierite appears as large clear invasive crystals in textural equilibrium with feldspar, locally enclosing internal schistosity marked by sillimanite fibers and containing ilmenite grains (Fig. 3a).

Sample *Ma3* thus records a multi-stage metamorphic history. Biotite, sillimanite and garnet are syn-kinematic minerals and constitute an early mineral paragenesis. Garnet and spinel are both contemporaneous to late compared to the foliation, which they both enclose and crosscut in several places. Feldspar and cordierite are post-kinematic minerals. The overgrowth of K-feldspar at alkali feldspar rims (Fig. 4a and g) as well as the presence of interstitial alkali feldspar enclosing euhedral porphyroblasts of spinel (Fig. 3b) suggest they grew from a melt, in equilibrium with cordierite.

4.2. Xenolith *Ma10*

Euhedral porphyroblasts of andalusite and garnet are dispersed in a matrix composed of feldspar, biotite, spinel and ilmenite (Fig. 3c and d) (Table 1). Andalusite shows a chistolitic form and appear surrounded by spinel and plagioclase coronas (Fig. 3c and d). In places, andalusite crystals are fractured and filled with the same mineral association as in the matrix (Fig. 3d; Fig. 4c and i). Rare corundum spreads in the matrix or appears enclosed in garnet or andalusite (Fig. 4c and i). Feldspars are either alkali feldspar or plagioclase. Plagioclase is observed at the rim or in the cracks of andalusite crystals (Fig. 4b, c, h and i). Plagioclase forms a continuous strip in contact with broken prisms of andalusite whereas K-rich feldspar is scattered in the middle of the fracture (Fig. 4c and i). Tiny crystals of orthoclase are included within the corona of cordierite around garnet. Sillimanite crosscuts and partly replaces andalusite

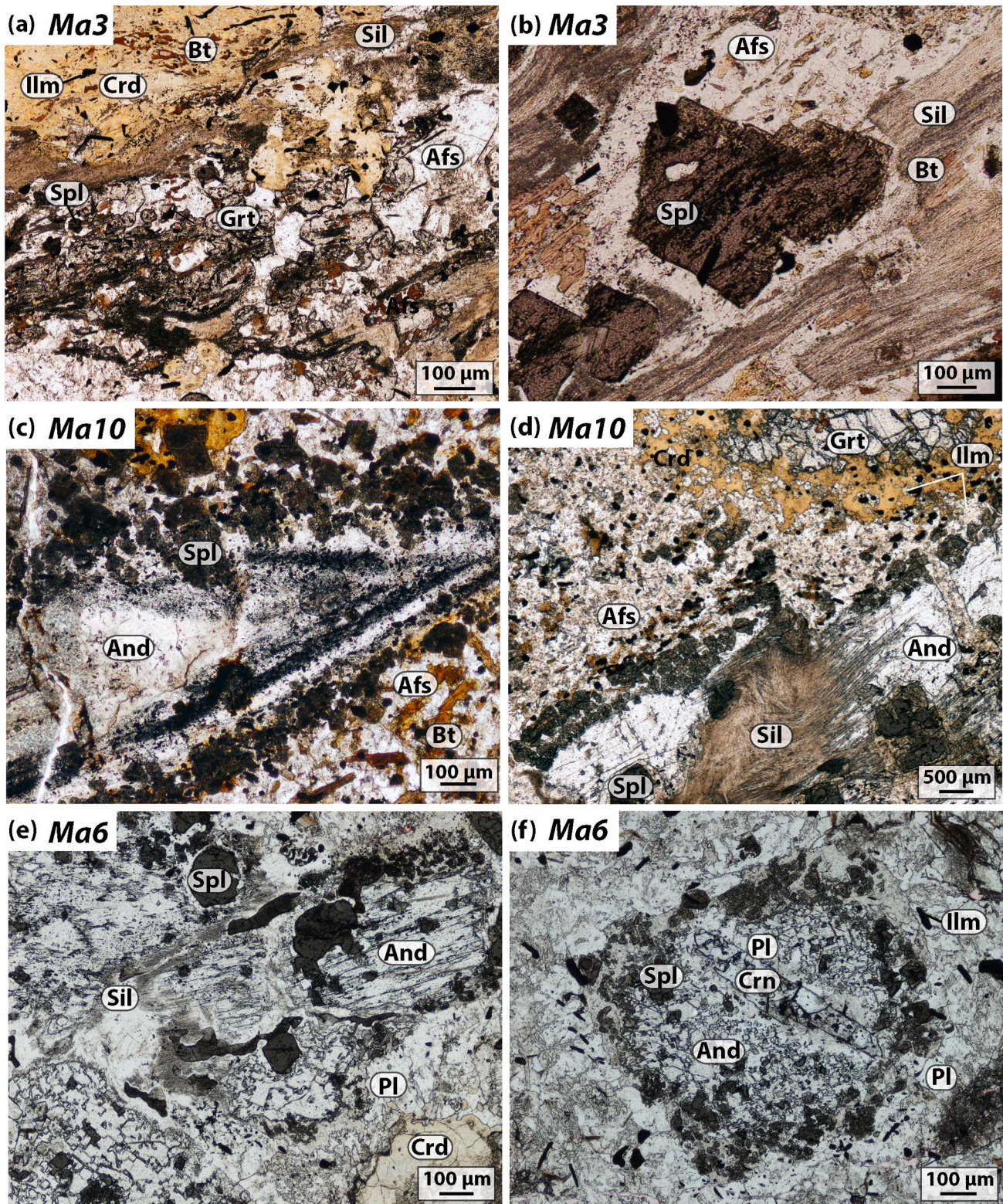


Fig. 3. Photomicrographs showing the assemblages and microstructures within the xenoliths. (a) *Ma3* Foliation underlined by sillimanite, skeletal biotite and elongated corroded garnet grains with sillimanite needles underlining and internal schistosity. Note the large cordierite flake enveloping all other mineral phases. (b) *Ma3* Note the presence of spinel overprinting the foliation. (c) *Ma10* Large chiascolitic andalusite prisms surrounded by a spinel + plagioclase corona. (d) *Ma10* Broken enbay crystal partly transformed into sillimanite and surrounded by a spinel-rich corona; cordierite corona surrounding garnet; plagioclase corona surrounding spinel. (e) *Ma6* Crystal of andalusite partially replaced by sillimanite and plagioclase; plagioclase contains spinel and separates andalusite from cordierite (f) *Ma6* Andalusite pseudomorph including corundum and transformed into plagioclase. (g) *Ma6* Plagioclase-spinel matrix displaying magmatic texture. (h) *Kar2b* Corundum and spinel within plagioclase replacing andalusite. (i) *Ma5* Plagioclase pseudomorphose of a crystal of andalusite (square section is recognizable). (j) *Ma5* Plagioclase euhedral twinned crystals with spinel inclusions. (k) *Ma5* Corundum rimmed by cordierite and spinel. (l) *Ma5* Corroded garnet grain rimmed by brown cordierite flakes. Mineral abbreviations from Whitney and Evans (2010).

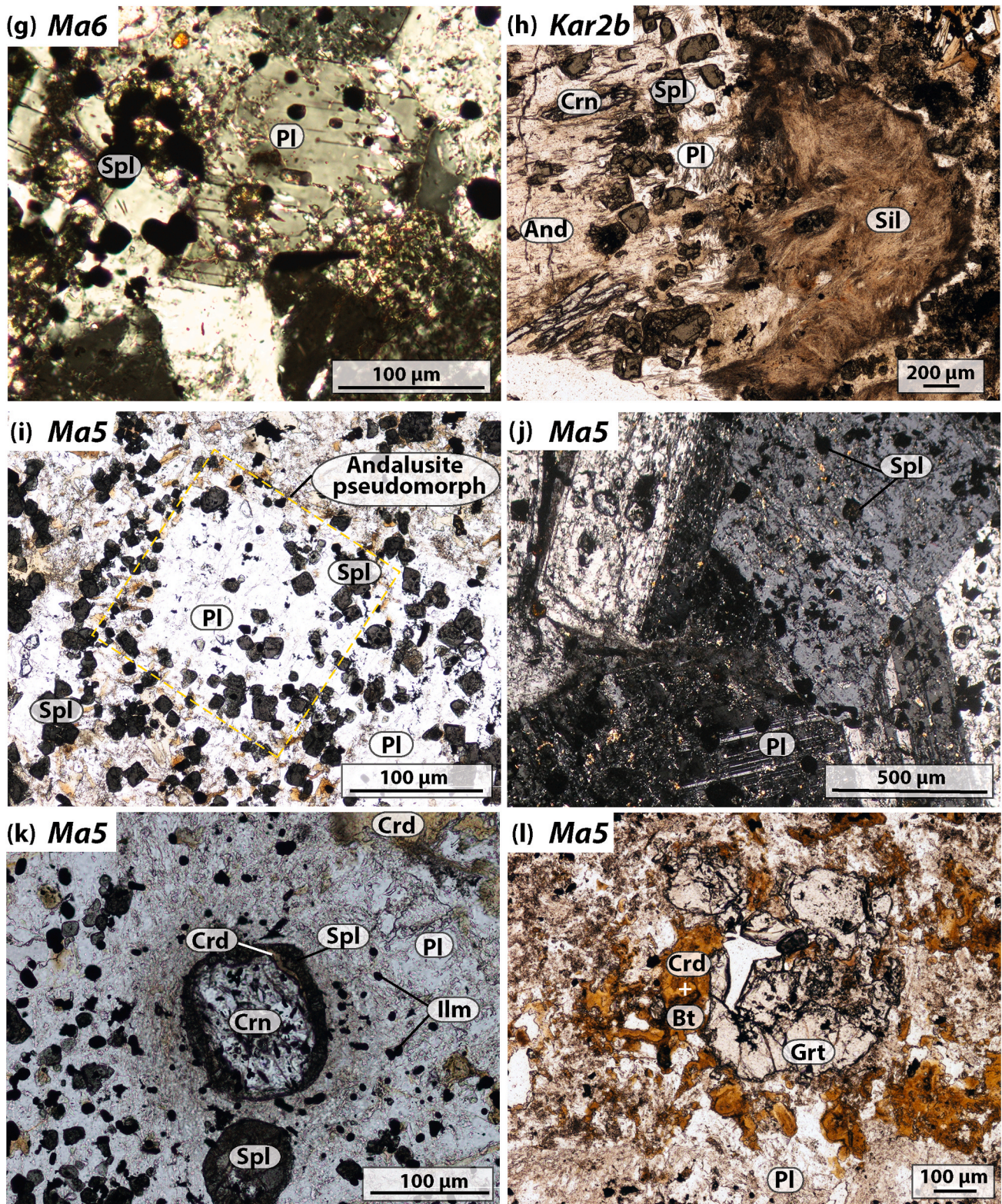


Fig. 3. (continued).

(Fig. 3d), locally also clearly crosscutting the feldspar bearing microcracks (not shown). Garnet crystals are rimmed by cordierite and alkali feldspar (Figs. 3d and 4b). Spinel occurs around and within andalusite crystals and as inclusion in feldspar (Fig. 3d).

To conclude, andalusite, garnet, corundum, alkali feldspar, biotite and ilmenite appear as an early mineral association, whereas

plagioclase, spinel, sillimanite and cordierite belong to later parageneses. Several lines of evidence account for the presence of a melt. These include i) the presence of feldspar-rich veinlets (Fig. 4c and i), ii) the clear spatial association of feldspar surrounding euhedral porphyroblasts of spinel in the vicinity of aluminosilicate, which is interpreted to record a melting reaction with spinel as peritectic product (e.g. Powell

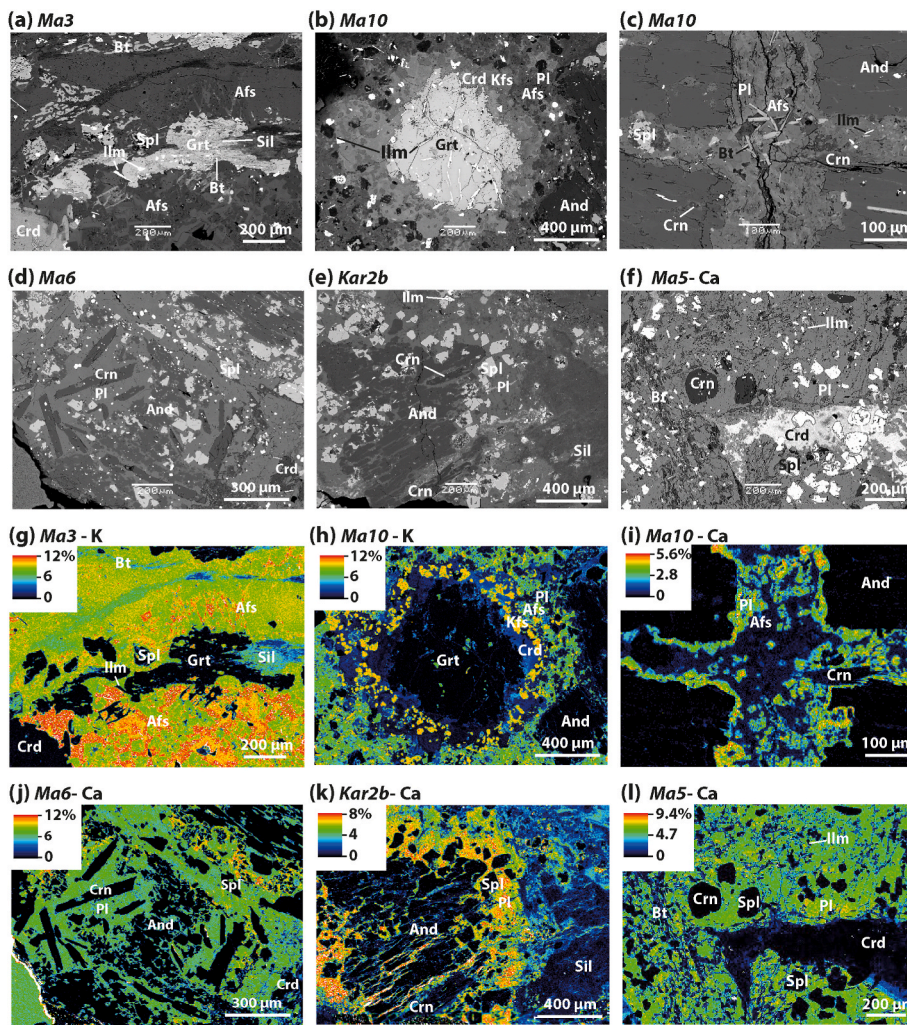


Fig. 4. BSE images and EDS maps of the xenoliths. (a, g) *Ma3*. Note oriented inclusions of sillimanite and ilmenite in garnet and the K enrichment at alkali feldspar boundaries (b) *Ma10* Feldspar – cordierite rims at garnet crystal. Note the complex alkali-feldspar/plagioclase concentric pattern (c) *Ma10* Plagioclase – alkali feldspar association filling microcracks in andalusite crystal (d) *Ma6* Andalusite crystals resorbed into a plagioclase – spinel association (e) *Kar2b* Andalusite crystals resorbed into a plagioclase – spinel association (f) *Ma5* Note resorbed corundum in a plagioclase matrix and the presence of cordierite. Quantitative EDS maps (g, j, k, l) have been used to quantify local composition for thermodynamical modelling. Mineral abbreviations from Whitney and Evans (2010).

and Downes, 1990; Johnson et al., 2004; Álvarez-Valero et al., 2007) (Fig. 3d), iii) the zoning pattern in plagioclase, characterized by an outwards decrease of the anorthitic content in the coronas surrounding andalusite crystals and a decrease of the anorthitic content away from the edges in the microfractures, which witnesses fractional growth from a liquid (Fig. 4i). iv) The presence of ternary feldspars (e.g. Or₂₀, An₁₅, Ab₆₅ (Fig. 5a) which suggest that they formed under partial melting conditions at ca. 900 °C (Elkins and Grove, 1990).

4.3. Xenoliths *Ma6* and *Kar2b*

Large euhedral fragmented crystals of andalusite are scattered in a fine-grained matrix of plagioclase (Fig. 3e) (Table 1). Andalusite is rimmed by a spinel-plagioclase association (Fig. 3e and f, Fig. 4d). Rare biotite (not shown) is scattered in the matrix. Acicular corundum appears as inclusions within andalusite (Fig. 3f and h; Fig. 4d). Locally, fibers of sillimanite develop upon andalusite (Fig. 3e and h). Large grains of cordierite are observed in the matrix, always separated from andalusite by a spinel-plagioclase association (Fig. 3e).

Thus, corundum and andalusite are considered as early mineral phases, whereas sillimanite, cordierite, plagioclase and spinel belong to later parageneses. The presence of plagioclase-spinel association at andalusite rim and the presence of interstitial anhedral plagioclase enclosing euhedral porphyroblasts of spinel (Fig. 3g) are interpreted as the witnesses of former partial melting reactions including spinel as a peritectic phase (e.g. Powell and Downes, 1990; Johnson et al., 2004; Álvarez-Valero et al., 2007).

4.4. Xenolith *Ma5*

Grey abundant spinel appears within large prisms of euhedral plagioclase (Fig. 3i and j; Table 1) and scattered in a matrix composed of plagioclase and rare and biotite (Fig. 3l) (Table 1). Corundum forms generally rounded crystals (Figs. 3k and 4f; Fig. 4l). Corroded garnet crystals (Fig. 3l) form isolated relics rimmed by cordierite and enclosing ilmenite. The rounded shape of garnet and corundum and the plagioclase matrix forming in places large euhedral crystals suggest the former presence of melt. Anhedral interstitial cordierite (Fig. 4f) forms around feldspar and some corundum crystals are rimmed by spinel and/or cordierite (Fig. 3k). This is broadly similar to sample *Ma10*, except for the absence of andalusite in sample *Ma5*. However, the former presence of andalusite is suggested by the squared shape of plagioclase-rich domains (Fig. 3i) that can be interpreted as pseudomorphs of andalusite crystals.

The early mineral paragenesis therefore comprises garnet, corundum, biotite and ilmenite, whereas spinel, cordierite and plagioclase belong to later parageneses. The presence of a former partial melt is indicated by i) the euhedral twinned plagioclase crystals (Fig. 3j), ii) the presence of interstitial anhedral plagioclase and/or alkali feldspar enclosing euhedral porphyroblasts of corundum (Fig. 3j and k), iii) rational crystal faces of feldspar crystals and iv) formation of overgrowths of spinel and cordierite on grains adjacent to feldspar (Fig. 3k) (Johnson et al., 2010).

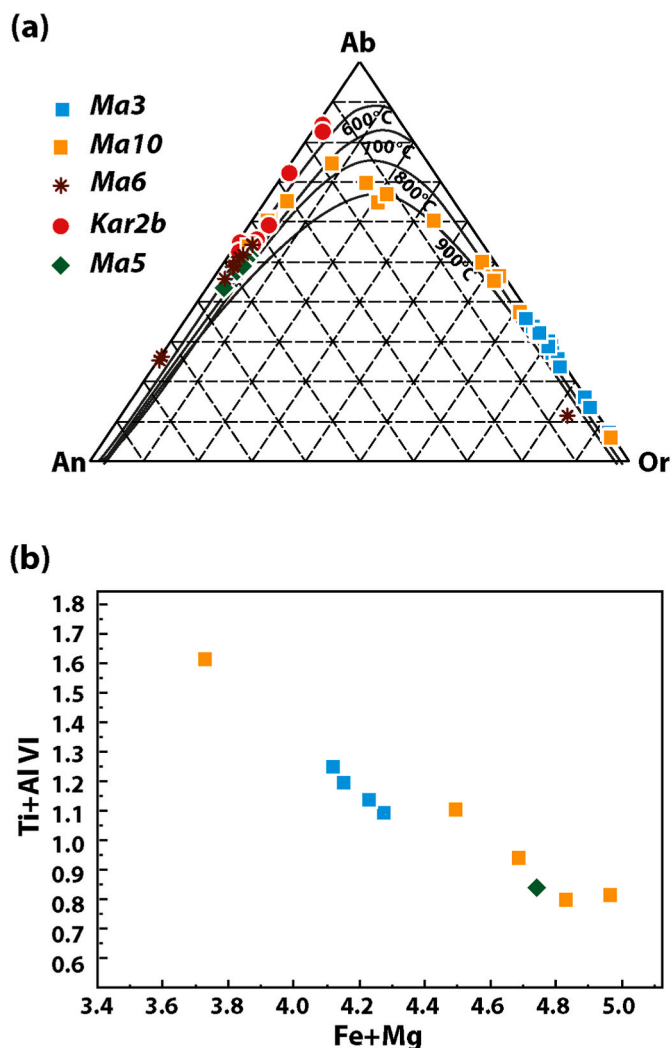


Fig. 5. Mineral chemistry a) Ternary diagram for feldspar with solvus isotherms at 5 kbar from Elkins and Grove (1990) (b) $Ti + Al^{VI} = f(Fe + Mg)$ diagram for biotite.

Table 2
Representative electron microprobe analyses of feldspars in xenoliths.

	Ma3	Ma3	Ma3	Ma10	Ma10	Ma10	Ma6	Ma6	Ma6	Kar2b	Kar2b	Kar2b	Ma5	Ma5	Ma5
SiO ₂	66.03	64.78	64.52	55.72	63.49	65.32	54.02	65.8	59.23	65.9	57.77	62.1	57.12	55.09	55.97
TiO ₂	0.00	0.28	0.06	0.03	0.11	0.00	0.00	0.07	0.00	0.09	0.18	0.14	0.03	0.06	0.02
Al ₂ O ₃	18.8	18.9	18.87	28.71	19.21	22.10	29.25	18.37	25.49	22.13	26.6	24.39	27.00	28.62	27.89
Fe ₂ O ₃	0.1	0.11	0.02	0.25	1.56	0.00	0.25	0.06	0.22	0.38	0.50	0.13	0.12	0.18	0.10
CaO	0.31	0.00	0.16	9.24	0.07	3.03	11.44	0.2	5.39	3.28	8.93	5.83	9.23	11.05	10.13
Na ₂ O	4.2	0.74	3.24	6.31	0.61	8.98	4.70	2.89	7.71	10.24	6.26	8.53	5.93	5.02	5.52
K ₂ O	10.93	15.32	11.73	0.46	14.35	1.21	0.34	12.55	1.02	0.20	0.57	0.19	0.65	0.49	0.59
Total	100.36	102.32	98.62	100.73	100.31	100.64	100.01	99.94	99.19	102.23	100.9	101.4	100.08	100.50	100.23
Si	2.99	2.99	3.03	2.58	2.96	3.01	2.51	3.05	2.79	3.01	2.67	2.86	2.65	2.55	2.59
Al	1.00	1.03	1.05	1.57	1.06	1.20	1.60	1.00	1.41	1.19	1.45	1.32	1.48	1.56	1.52
Ti	0.00	0.01	0.00	0.00	0.00	0.00	0.00	0.00	0.00	0.00	0.01	0.00	0.00	0.00	0.00
Fe ²⁺	0.00	0.00	0.00	0.01	0.05	0.00	0.01	0.00	0.01	0.01	0.02	0.00	0.00	0.01	0.00
Ca	0.02	0.00	0.01	0.46	0.00	0.15	0.57	0.01	0.27	0.16	0.44	0.29	0.46	0.55	0.50
Na	0.37	0.00	0.00	0.00	0.00	0.00	0.00	0.00	0.00	0.00	0.00	0.00	0.00	0.00	0.00
K	0.63	0.90	0.70	0.03	0.85	0.07	0.02	0.74	0.06	0.01	0.03	0.01	0.04	0.03	0.03
Ab	36.32	6.84	29.33	53.84	6.05	78.42	41.79	25.67	67.87	84.04	54.11	71.82	51.75	43.85	47.97
An	1.48	0.00	0.80	43.57	0.38	14.62	56.22	0.98	26.22	14.88	42.65	27.13	44.52	53.34	48.65
Or	62.20	93.16	69.87	2.58	93.57	6.95	1.99	73.35	5.91	1.08	3.24	1.05	3.72	2.82	3.37

Chemical formulae were calculated on the basis of 8 oxygens.

5. Mineral chemistry

5.1. Feldspars

In xenolith *Ma3*, only alkali-feldspar is present and crystals present chemical zoning (Or 62–90 mol.%, Table 2, Fig. 5a). Alkali-feldspar domains are formed by Na-rich crystals with interstitial K-rich domains (Fig. 4g). In xenolith *Ma10*, feldspars composition is highly variable from plagioclase (An 35–45 mol.%) to alkali feldspar (Or 47–92 mol.%) with several intermediate ternary feldspar compositions (Table 2, Figs. 4h and 5a). Feldspar in xenoliths *Ma6* and *Kar2b* is mainly plagioclase (An 26–74 mol.% and 15–45 mol.% respectively, Table 2, Fig. 5a) associated with corundum and spinel in replacement of andalusite (Fig. 4j and k). Rare alkali feldspar (Or 57–88 mol.%) is also present in sample *Ma6*. In xenolith *Ma5*, feldspar is a homogeneous (Table 2, Fig. 4l and 5a), with An content comprised between 45 and 53 mol.%.

5.2. Spinel

Most of crystals of spinel are grey and belong to hercynitic spinel (Table 3). X_{Fe} varies from sample to sample but appears mostly homogeneous in each xenolith. The lowest X_{Fe} (0.57–0.64) is observed in xenolith *Ma5*, the highest in xenolith *Ma6* (0.70–0.74), whereas it is intermediate in samples *Ma3* (0.67–0.72), *Ma10* (0.63–0.79) and *Kar2b* (0.64–0.69). The ZnO content reaches 0.5 wt%.

5.3. Garnet

Garnet is present in xenoliths *Ma3*, *Ma10* and *Ma5*. They are almandine-pyrope garnets, with composition ranging from $X_{Alm} = 64$ –73% in *Ma3* and from $X_{Alm} = 59$ –67% in *Ma10* (Table 4). Garnet from *Ma10* is generally spessartine - richer than garnet from *Ma3* (X_{Sps} up to 6%), with spessartine content presenting typical bell-shaped profile (not shown).

5.4. Biotite

Biotite is generally Ti-rich (TiO₂ 3 to 7 wt% in *Ma10* and up to 8 wt% in *Ma3*) (Table 4, Fig. 5b). The lowest TiO₂ is observed in sample *Ma5* (TiO₂ < 5 wt%). X_{Mg} varies from 0.45 in *Ma3*, 0.4 to 0.56 in *Ma10* and 0.49 to 0.56 in *Ma5*.

Table 3
Representative electron microprobe analyses of spinel in xenoliths.

	Ma3	Ma3	Ma10	Ma10	Ma6	Ma6	Kar2b	Kar2b	Ma5	Ma5
SiO ₂	0.13	0.05	0.08	0.21	0.22	0.15	0.19	0.03	0.04	0.19
TiO ₂	0.21	0.26	0.34	0.36	0.14	0.19	0.32	0.37	0.21	0.42
Al ₂ O ₃	60.01	59.23	61.14	62.47	59.38	60.64	60.43	60.57	60.51	60.84
Cr ₂ O ₃	0.04	0.13	0.07	0.17	0.04	0.06	0.03	0.04	0.17	0.09
Fe ₂ O ₃	1.00	2.51	1.05	0.00	0.92	0.00	0.93	0.96	1.48	0.21
FeO	29.31	29.04	27.84	29.59	31.52	29.59	30.08	27.87	24.66	27.98
MnO	0.00	0.04	0.25	0.24	0.27	0.34	0.53	0.40	0.20	0.23
MgO	7.72	7.88	9.05	8.47	6.32	7.22	7.43	8.76	10.56	8.80
ZnO	0.00	0.00	0.11	0.15	0.00	0.53	0.22	0.00	0.07	0.33
Total	98.42	99.14	99.93	101.66	98.81	98.72	100.15	99.00	97.90	99.09
Si	0.00	0.00	0.00	0.01	0.01	0.00	0.01	0.00	0.01	0.00
Ti	0.01	0.01	0.01	0.01	0.00	0.00	0.01	0.01	0.01	0.01
Al VI	1.97	1.93	1.96	1.97	1.96	1.97	1.96	1.96	1.96	1.96
Cr	0.00	0.00	0.00	0.00	0.00	0.00	0.00	0.00	0.00	0.00
Fe ³⁺	0.02	0.05	0.02	0.00	0.02	0.01	0.02	0.02	0.02	0.02
Fe ²⁺	0.68	0.67	0.63	0.66	0.74	0.69	0.69	0.64	0.69	0.64
Mn ²⁺	0.00	0.00	0.01	0.01	0.01	0.01	0.01	0.01	0.01	0.01
Mg	0.32	0.33	0.37	0.34	0.26	0.30	0.30	0.36	0.30	0.36
Zn	0.00	0.00	0.00	0.00	0.00	0.01	0.00	0.00	0.00	0.00
XFe ²⁺	0.68	0.67	0.63	0.66	0.74	0.70	0.69	0.64	0.69	0.64

Chemical formulae were calculated on the basis of 4 oxygens.

Table 4
Representative electron microprobe analyses of garnet and biotite in xenoliths.

	Garnet				Biotite							
	Ma3	Ma3	Ma10	Ma10	Ma3	Ma3	Ma3	Ma10	Ma5	Ma5	Ma5	
SiO ₂	39.00	37.45	37.94	37.23	SiO ₂	34.62	36.23	34.67	36.05	35.4	35.17	36.17
TiO ₂	0.21	0.18	0.14	0.39	TiO ₂	7.98	6.21	8.14	4.29	5.15	3.77	4.91
Al ₂ O ₃	21.98	20.88	22.4	21.04	Al ₂ O ₃	17.33	16.18	16.71	16.81	15.56	17.15	15.71
Cr ₂ O ₃	0.09	0.00	0.00	0.00	Cr ₂ O ₃	0.01	0.18	0.3	0.06	0	0.02	0.08
Fe ₂ O ₃ (c)	0.19	0.91	1.49	1.06	FeO	16.87	18.45	17.68	17.23	18.81	17.35	18.13
FeO	30.37	32.61	26.85	31.05	MnO	0.07	0.09	0	0.21	0.02	0	0.1
MnO	0.57	0.35	1.60	2.69	MgO	8.8	8.6	8.89	11.12	10.19	12.28	11.34
MgO	8.62	6.14	8.57	5.86	CaO	0	0.03	0.06	0.02	0	0.1	0.15
CaO	0.4	0.81	1.36	1.32	Na ₂ O	0.37	0.45	0.44	0.47	0.56	0.5	0.43
Total	101.42	99.33	100.35	99.66	K ₂ O	8.78	8.98	8.71	8.28	8.99	8.27	8.41
					BaO	0.11	0.18	0.23	0.47	0	0.6	0.35
Si	2.99	2.98	2.93	2.96	NiO	0.04	0	0.06	0	0.04	0.08	0
Ti	0.01	0.01	0.01	0.02	F	1.24	1.28	1.76	1.22	2.64	1.93	2.02
Al IV	0.01	0.02	0.07	0.04	Cl	0.15	0.25	0.16	0.28	0.78	0.21	0.65
Al VI	1.97	1.94	1.97	1.93	Total	96.37	97.11	97.81	96.51	98.14	97.43	98.45
Cr	0.01	0.00	0.00	0.00	Si	2.585	2.703	2.566	2.686	2.629	2.604	2.660
Fe ³⁺	0.01	0.05	0.09	0.06	Ti	0.448	0.349	0.453	0.240	0.288	0.210	0.272
Fe ²⁺	1.95	2.17	1.73	2.00	Al IV	1.415	1.297	1.434	1.314	1.362	1.396	1.340
Mn ²⁺	0.04	0.02	0.11	0.18	Al VI	0.110	0.125	0.024	0.163	0.000	0.101	0.022
Mg	0.98	0.73	0.99	0.69	Fe ²⁺	1.054	1.151	1.094	1.074	1.168	1.074	1.115
Ca	0.03	0.07	0.11	0.11	Mn ²⁺	0.004	0.006	0.000	0.013	0.001	0.000	0.006
Pyrope	32.80	24.00	33.59	23.00	Mg	0.980	0.956	0.981	1.235	1.128	1.355	1.243
Almandin	64.87	73.00	59.02	67.00	Ca	0.000	0.002	0.005	0.002	0.000	0.008	0.012
Spessartine	1.24	1.00	3.56	6.00	Na	0.054	0.065	0.063	0.068	0.081	0.072	0.061
Andradite	0.54	0.00	3.83	0.00	K	0.836	0.855	0.822	0.787	0.852	0.781	0.789
Uvarovite	0.27	0.00	0.00	0.00	Ba	0.003	0.005	0.007	0.014	0.000	0.017	0.010
Grossulaire	0.29	2.00	0.00	4.00	Ni	0.002	0.000	0.004	0.000	0.002	0.005	0.000
XMg	0.34	0.26	0.36	0.24	F	0.293	0.302	0.412	0.287	0.620	0.452	0.470
					Cl	0.019	0.032	0.020	0.035	0.098	0.026	0.081
					XMg	0.482	0.454	0.473	0.559	0.491	0.558	0.527

Chemical formulae were calculated on the basis of 12 oxygens for garnet and 11 oxygens for biotite.

6. Petrological and geochemical relationships between host rocks and xenoliths

6.1. Host rocks and xenolith contacts

The microgranodiorite host rock has a porphyritic texture with

phenocrysts of plagioclase, amphibole, biotite and quartz in a fine-grained matrix composed of quartz, plagioclase, K-feldspar and rare biotite (Fig. 6a). In sample *Ma3* (Fig. 6b), the contact is sharp. A few xenocrysts of biotite from the xenolith are nevertheless present in the host rock near the contact, accounting for mechanical exchange between the host magma and the xenolith. In sample *Ma10* (Fig. 6c), the contact

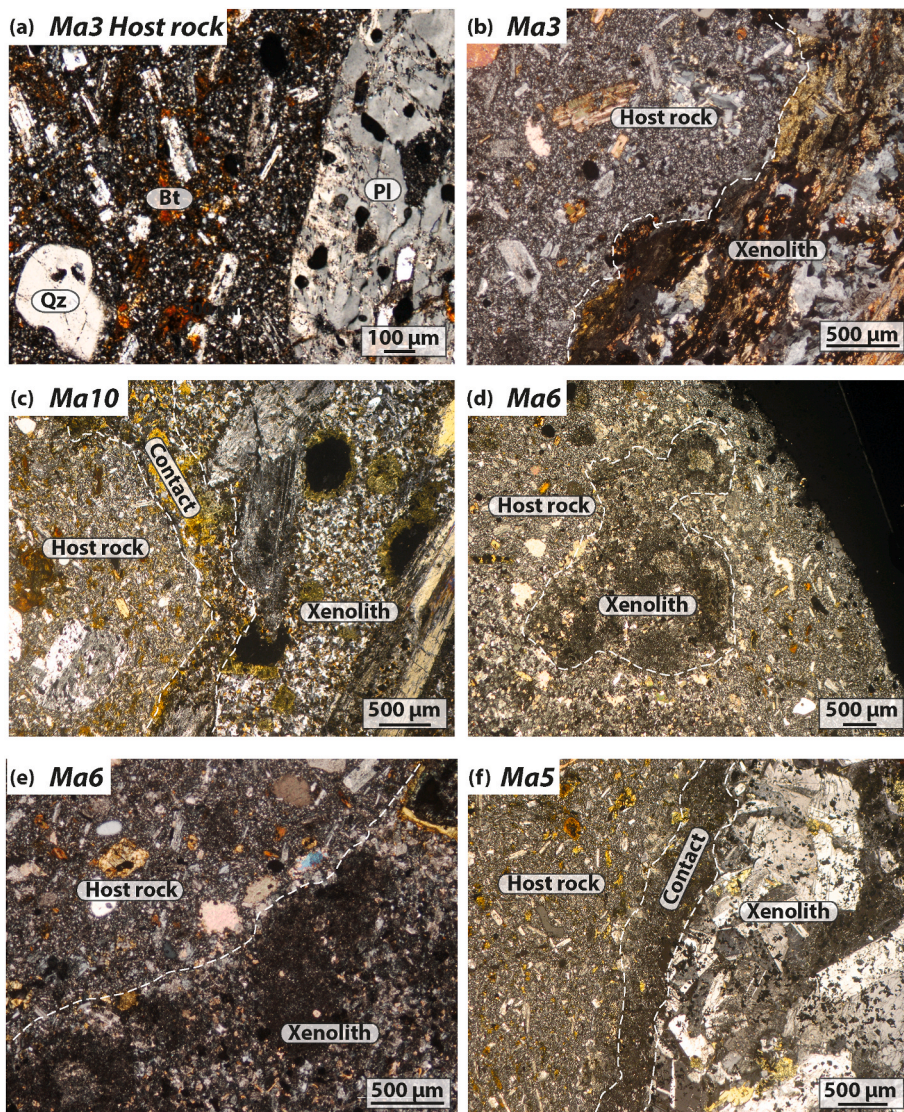


Fig. 6. Photomicrographs of the host rock and contacts with the xenoliths (a) *Microgranodioritic host rock*. Note the porphyritic texture with phenocrysts of plagioclase, amphibole, biotite and quartz in a fine-grained matrix composed of quartz, plagioclase, K-feldspar and rare biotite. (b) *Ma3* Sharp contact, with a few xenocrysts of biotite from the xenolith in the host rock. (c) *Ma10* Sharp contact between xenolith and host rock underlined by a two mm large zone where abundant pinnite replaces cordierite. (d, e) *Ma6* Host rock/xenolith contact underlined by the presence of large andalusite crystals sometimes fully enclosed in the host rock. (f) *Ma5* Host rock/xenolith contact marked a localized (<1 mm large) chloritized band. Mineral abbreviations from Whitney and Evans (2010).

is characterized by a two mm large rim along the xenolith limit where abundant pinnite replaces cordierite. In sample *Ma6*, the contact is underlined by the presence of large andalusite crystals broadly similar to those of the core of the xenoliths and preserving spinel relics (Fig. 6d and e). Such andalusite crystals are sometimes fully enclosed in the host rock, featuring mechanical exchange between the host magma and the xenolith. In sample *Ma5* (Fig. 6f), the contact is sharp, with a two mm large rim along the xenolith limit. In the rim, the host rock is characterized by reduced crystal size, the lack of phenocrysts, and the absence of biotite.

6.2. Geochemistry of host rocks and xenoliths

Major and trace elements have been analyzed in the xenoliths and their host rocks (Table 5). Xenoliths have a low to intermediate SiO_2 content of 44–57 wt% (Table 5, Fig. 7a). They are characterized by a high although variable Al_2O_3 content (18–34 wt%) that reaches very high values ($ca. > 30\%$) in the silica poorer samples. Alkali content is high ($5 < \text{Na}_2\text{O} + \text{K}_2\text{O} < 9$ wt%). Host rocks have a SiO_2 content of 62–68 wt% (Table 5). In the SiO_2 – $\text{Na}_2\text{O} + \text{K}_2\text{O}$ diagram (Fig. 7b and Cox et al., 1979), 6 samples fall in the field of quartz diorite. One sample, *2Kar 8*, coming from a different dyke, has the composition of a granite. Compared to the host rock, the xenoliths are enriched in a number of

trace elements (Figs. 8a and 9), notably HFSE (Nb, Ti) and some of the transition elements (Cr, V, W, Ni). By contrast, there is no element for which there is a systematic enrichment of the host rock compared to the xenolith.

Host rocks present very similar decreasing REE spectra, with $(\text{La}/\text{Yb})_N$ in the range 13–16 (Figs. 8b and 9a). The microgranitic sample *2Kar 8* presents a slight Eu anomaly. Xenolith samples also display decreasing REE spectra, broadly parallel, either above or below the host-rock spectra, with 5 samples presenting $(\text{La}/\text{Yb})_N$ values similar to that of the host rock and 4 samples presenting $(\text{La}/\text{Yb})_N$ scattered between 5 and 30 (Fig. 8b). Note that the $(\text{La}/\text{Yb})_N$ ratio is not correlated to the SiO_2 content of the xenolith. The overall REE content varies by an order of magnitude in the xenoliths, the more enriched samples (*Ma3*, *Ma10*, *Ma5*, *2Kar5*, *Kar2b*) having the lowest SiO_2 content (44–51 wt%). The extended spectra highlight negative anomalies for both the host rocks and the xenoliths in Nb, Ta, Ti and P, and a positive anomaly in Pb. No correlation was found between the chemical composition of the host rock and corresponding xenolith.

Table 5

Whole rock analyses of selected host rocks and xenoliths (Major elements in wt.%, trace elements in ppm).

	Host rocks		Xenoliths										
	Kar2b	2Kar8	Kar2b	Kar 7	2Kar 2	2Kar 3	2Kar 4	2Kar 5	2Kar 8	Ma6	Ma5	Ma3	Ma10
SiO ₂	67.58	70.76	44.99	57.01	54.03	56.47	53.76	51.25	55.84	56.24	51.51	46.76	44.07
Al ₂ O ₃	15.49	15.11	30.99	21.46	20.39	20.12	22.22	27.39	17.58	24.91	29.29	20.26	33.84
Fe ₂ O ₃	5.15	2.74	9.41	6.22	8.75	8.98	8.08	5.92	12.66	5.31	6.01	9.55	6.20
MnO	0.22	0.04	0.25	0.24	0.16	0.18	0.10	0.15	0.12	0.11	0.22	0.15	0.13
MgO	1.82	1.00	2.67	2.37	3.17	4.33	2.55	2.26	4.15	1.78	1.57	3.31	1.74
CaO	2.37	2.34	2.94	2.88	4.62	1.97	4.04	2.13	2.91	3.40	1.53	3.58	0.67
Na ₂ O	3.18	3.57	2.98	2.68	3.49	4.01	4.45	3.86	2.82	3.49	2.60	2.74	1.94
K ₂ O	3.39	3.94	3.98	5.62	3.25	2.69	3.69	5.17	1.78	3.25	5.36	4.38	4.29
TiO ₂	0.60	0.36	1.56	1.41	1.78	1.15	1.03	1.60	1.95	1.42	1.81	1.22	2.00
P ₂ O ₅	0.20	0.14	0.23	0.10	0.37	0.09	0.08	0.28	0.19	0.10	0.12	1.36	0.09
L.O.I	2.62	3.38	3.22	3.25	6.45	4.35	2.16	3.86	5.81	7.93	3.62		
Ba	812	842	895	1531	260	725	1126	1724	603	1426	2954	1108	2390
Be	2.41	3.05	5.60	4.00	2.62	2.70	2.79	4.33	3.47	10.87	7.92	4.77	10.03
Cd	16.82	0.48	1.56	1.23	0.58	2.03	0.31	0.34	1.50	0.25	0.42	0.52	0.16
Ce	65.03	60.44	105.80	72.16	31.31	56.36	99.05	133.10	37.03	69.62	191.70	124.10	151.70
Co	21.44	4.16	19.09	11.74	29.04	24.20	16.83	14.15	16.92	13.27	19.60	25.04	18.59
Cr	25.10	16.86	143.90	149.50	57.32	84.55	90.22	142.90	112.0	100.90	160.90	91.68	167.20
Cs	2.71	2.37	7.23	3.07	10.52	2.72	3.70	9.43	2.66	12.86	6.98	6.82	6.36
Cu	17.77	9.41	6.00	8.78	6.27	18.66	18.26	0.00	40.17	14.38	7.84	7.01	5.82
Dy	3.37	3.15	5.54	2.90	2.94	2.57	3.25	7.07	3.00	2.32	7.70	15.10	9.02
Er	1.77	1.66	2.83	1.35	1.79	1.27	1.15	3.59	1.56	1.14	4.05	7.43	5.01
Eu	1.11	0.84	1.79	1.85	0.90	1.31	2.14	2.38	1.73	1.50	3.72	3.75	3.73
Ga	20.52	20.20	37.71	28.55	28.21	28.76	32.22	34.25	34.53	29.58	33.02	26.96	40.14
Gd	4.01	3.73	6.73	4.15	2.92	3.33	4.91	8.02	3.35	3.19	9.87	17.63	9.40
Ge	1.45	1.34	1.90	1.58	1.55	1.65	1.88	2.19	1.74	2.04	3.01	2.00	4.50
Hf	4.56	4.59	6.92	5.12	3.72	8.27	7.24	7.69	3.42	5.94	8.51	20.46	8.48
Ho	0.68	0.62	1.09	0.53	0.67	0.49	0.51	1.38	0.62	0.44	1.52	2.76	1.76
La	32.77	30.12	53.55	34.47	14.25	27.73	48.09	66.34	18.48	34.49	89.82	54.26	76.65
Lu	0.26	0.25	0.43	0.21	0.26	0.21	0.18	0.53	0.18	0.18	0.60	1.09	0.80
Mo	3.70	0.00	1.22	0.66	1.78	1.22	1.03	5.15	0.00	0.80	0.89	0.50	0.52
Nb	8.89	8.20	22.32	19.87	13.94	22.19	20.45	23.92	29.03	14.03	23.70	19.07	21.88
Nd	26.86	24.64	45.64	30.20	14.93	22.70	38.62	55.05	16.25	26.83	82.41	61.38	64.28
Ni	40.64	10.95	45.82	37.63	39.26	57.29	32.79	27.70	47.96	30.10	30.30	35.97	55.67
Pb	431.85	51.84	142.78	542.61	43.15	151.1	39.06	30.79	299.0	11.57	43.81	41.64	22.47
Pr	7.33	6.74	12.28	8.05	3.73	6.16	10.76	14.91	4.09	7.46	21.78	15.25	17.46
Rb	103.60	128.1	148.60	136.90	201.3	104.8	151.20	147.30	76.03	137.70	185.50	189.90	169.00
Sm	4.91	4.71	8.39	5.82	3.15	4.37	6.77	10.23	3.66	4.51	15.09	16.35	11.43
Sr	360.1	263.1	387.8	652.9	316.4	573.6	464.3	477.7	214.5	350.8	545.0	312.7	377.0
Ta	0.99	1.03	2.00	1.73	1.33	1.65	1.58	2.06	1.91	1.29	2.47	1.73	2.40
Tb	0.58	0.53	0.94	0.55	0.45	0.46	0.64	1.22	0.49	0.43	1.36	2.68	1.50
Th	13.07	15.44	15.88	10.89	5.13	16.30	20.07	21.83	6.03	7.89	24.65	18.77	22.16
U	6.51	5.88	3.16	4.18	3.19	4.79	3.46	4.03	4.10	2.58	4.00	5.81	3.62
V	62.05	32.99	204.1	192.9	162.2	99.54	124.8	205.2	182.6	156.3	216.8	140.5	234.0
W	1.59	0.41	2.94	4.91	2.94	2.65	1.40	22.49	2.17	1.94	1.62	2.74	1.66
Y	18.41	18.34	27.05	13.63	17.70	13.18	12.13	35.19	18.43	11.57	37.15	79.46	45.80
Yb	1.68	1.59	2.73	1.27	1.68	1.28	1.08	3.39	1.25	1.10	3.96	7.22	5.16
Zn	1636.0	73.21	776.1	348.7	154.4	260.1	257.6	339.2	440.3	123.3	120.6	200.4	244.0
Zr	174.20	160.10	246.60	179.00	154.80	299.50	255.40	287.10	129.60	224.20	307.10	685.50	301.50
ΣREE	529	487	873	570	305	451	735	1083	352	522	1495	1317	1297

7. Mineral equilibria modeling

7.1. Ma3 xenolith

A pseudosection has been drawn for the local composition of a microdomain in sample *Ma3* (EDS map Figs. 6a and 10). The microdomain is fully representative of the mineral assemblages at the thin section scale. The mineral assemblage (biotite + melt + plagioclase + K-feldspar + spinel + garnet + sillimanite + ilmenite) is stable in the pseudosection for a temperature range of 850–900 °C and for a pressure higher than 5 kbar. Isopleths curves for garnet and biotite are reported in the pseudosection and are in agreement with such *PT* range. They define a narrow range between 850 and 915 °C. Modes at this temperature correspond to K-feldspar 50 wt%, biotite 10 wt%, garnet 15 wt%, ilmenite 5 wt%, melt 10 wt%, plagioclase <5 wt%, sillimanite <5 wt% and spinel 5 wt%, in agreement with petrographic observations. The fraction of melt calculated at 850–900 °C is estimated as 15–25%. Partial melting may have started at a temperature of *ca.* 725 °C in the stability

field of garnet and sillimanite for a pressure above 5 kbar. The presence of cordierite accounts for a decompression below 5 kbar. These characteristics are accounted for by a prograde path at a pressure above 5 kbar from 725 to 850–900 °C, followed by a decompression path toward lower pressure and temperature conditions, as shown in Fig. 10.

7.2. Ma10 xenolith

The pseudosection (Fig. 11) for sample *Ma10* has been calculated for whole rock composition (recalculated from Table 5 for a water content of 0.54 wt% determined from *T-X*_{H₂O} section) since none of the microdomain was representative of the sample. In the pseudosection the mineral assemblage (biotite + cordierite + plagioclase + K-feldspar + garnet + spinel + sillimanite + ilmenite + melt) is reached for temperatures between ~800 and 850 °C and pressures between 4 and 6 kbar. The upper and lower temperatures are constrained by the presence of biotite and spinel in the mineral assemblage respectively, whereas pressure is constrained by the garnet-cordierite stability field. The

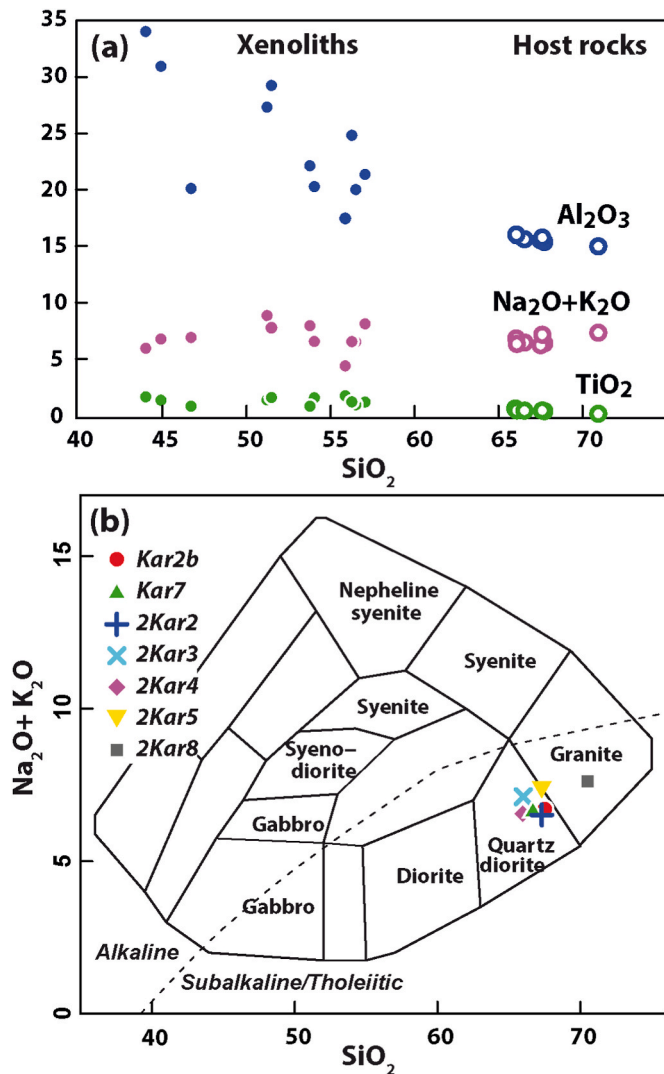


Fig. 7. Major element characteristics of xenoliths and host rocks (a) Harker diagrams showing Al₂O₃, Na₂O + K₂O and TiO₂ variation as a function of SiO₂ (b) Cox classification diagram for plutonic rocks (Cox et al. 1979), plotted with GCDKit software (Janoušek et al., 2006). Note that sample Kar2b corresponds to the host rock of the corresponding studied xenolith.

isopleths for plagioclase, biotite and garnet compositions better constrain the temperature to ~850 °C (Fig. 11). Modes at 850 °C correspond to biotite 15 wt%, plagioclase 10 wt%, K-feldspar 20 wt%, sillimanite 30 wt%, garnet 10 wt%, cordierite <5 wt%, spinel <5 wt%, melt <5 wt% and ilmenite <5 wt%, and are in agreement with petrographic observations. In addition, the observations of i) corroded garnet grains and cordierite growth in the presence of biotite and spinel and ii) spinel at andalusite/sillimanite rims (Fig. 3c) indicate a temperature increase above 4 kbar to reach the peak *PT* conditions. Andalusite chistolite attests for an early metamorphism (*PT* conditions outside of the range of the pseudosection). Sillimanite may have grown at the expense of andalusite during heating. Sillimanite fibers crosscutting the feldspar-rich veins and the modes calculated from the model (Supplemental material 2) suggest as an alternative that cooling may then have produced both crystallization of feldspar from the melt and growth of sillimanite fibers fringing andalusite crystals.

7.3. Ma6 xenolith

The composition of a microdomain (Fig. 4d and j), silica poor and alumina rich, has been used to compute a pseudosection (Fig. 12). It is

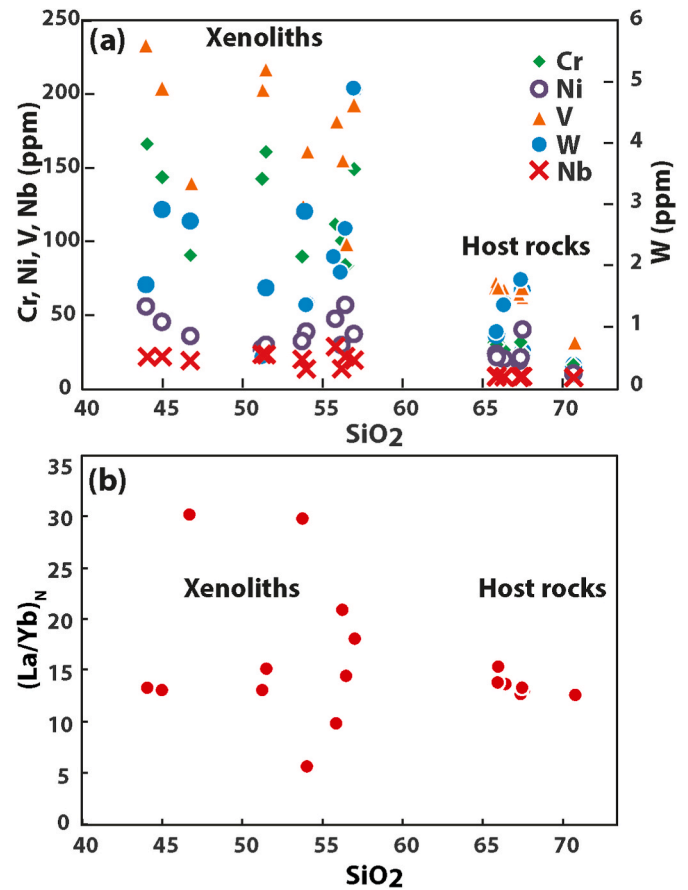


Fig. 8. Trace element characteristics of xenoliths and host rocks (a) Harker diagrams showing selected transition element variation as a function of SiO₂. (b) La/Yb as a function of SiO₂.

representative in terms of petrographic characteristics of the sample at the thin section scale. The H₂O content was fixed to be just low enough to account for the absence of biotite at the solidus, in order to match the observations, *i.e.* no biotite on the microdomain and rare biotite at the xenolith scale. In the pseudosection, partial melting takes place above 800 °C thanks to the consumption of K-feldspar and, at low pressure (<3 kbar) produces small amounts of spinel (*e.g.* Fig. 3g) while consuming cordierite (Supplemental material 3). The observed assemblage corresponds to temperatures higher than 900 °C, as constrained by partial melting and the absence of K-feldspar. Modes at 900 °C correspond to plagioclase 30 wt%, corundum 15 wt%, cordierite 20 wt%, melt 10 wt%, spinel 10 wt%, K-feldspar 5 wt%; sillimanite 10 wt% and ilmenite <0.4 wt%, in agreement with petrographic observations. Moreover, the presence of andalusite resorbed and rimmed by a spinel – plagioclase association accounts for an initial metamorphic stage at a temperature lower than 700 °C and a pressure lower than 2 kbar. Andalusite then remains in a metastable state, without being replaced by sillimanite in this microdomain. To summarize, sample Ma6 thus record partial melting at low pressure (<2 kbar) with a temperature increase from less than 700 °C to more than 900 °C.

7.4. Kar2b xenolith

The composition corresponding to the microdomain of Fig. 4e and k, silica poor and alumina rich, has been used to compute the pseudosection of Fig. 13. The petrographical features are representative of the sample at the sample scale. The H₂O content was fixed to be just low enough to account for the absence of biotite at the solidus, in order to match the observations, *i.e.* no biotite on the microdomain and rare

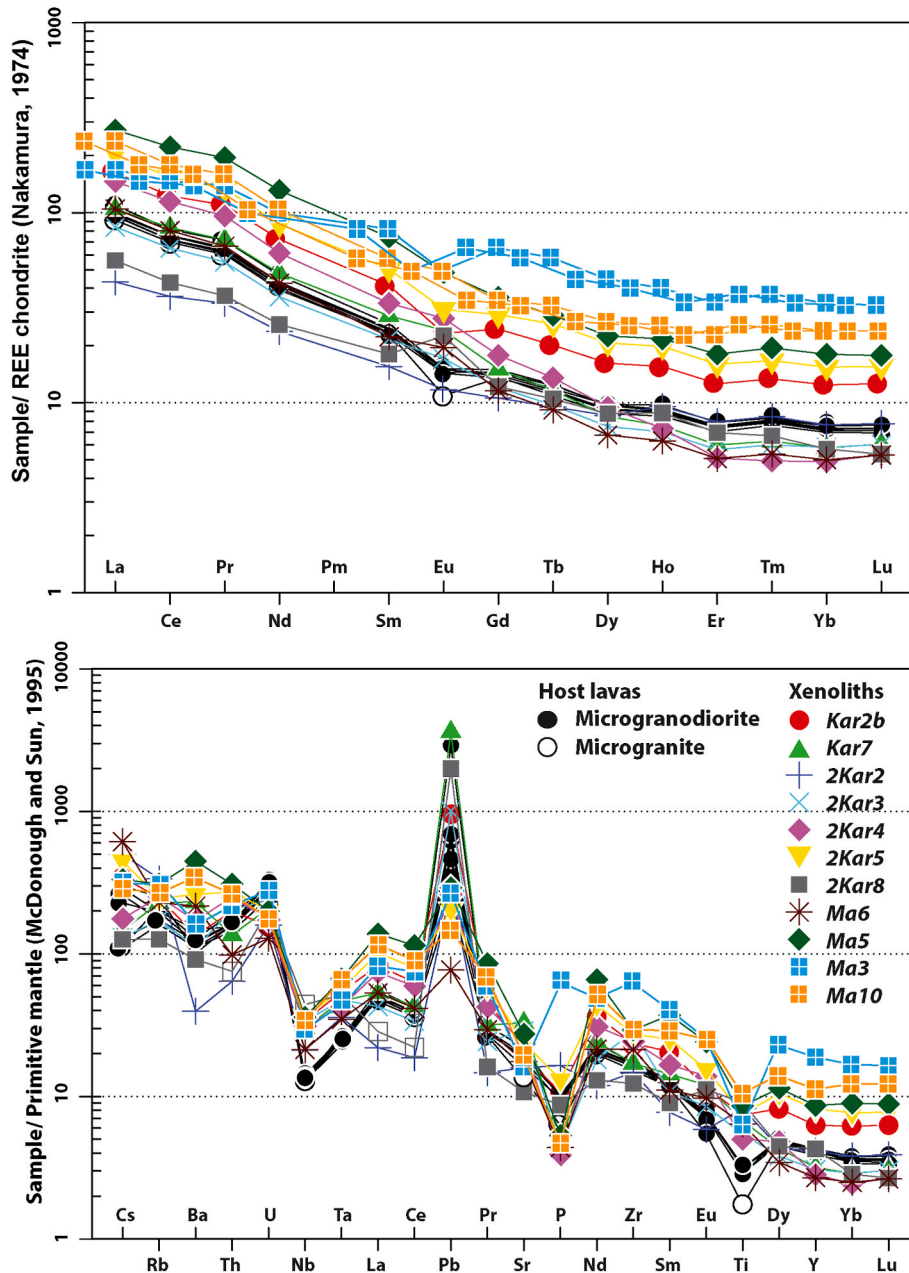


Fig. 9. Spidergrams for xenoliths and host rocks (a) REE elements normalized to chondrite (Nakamura, 1974) (b) Trace element spectra normalized to primitive mantle (McDonough and Sun, 1995). Diagrams plotted with GCDKit software (Janoušek et al., 2006).

biotite at the xenolith scale.

The absence of K-feldspar suggests its almost total consumption by partial melting reaction at *ca.* 900 °C, whereas the absence of garnet constrains pressure to below 4 kbar (Fig. 13). At such low pressure, partial melting would produce spinel (Fig. 3h) at the expense of cordierite (Supplemental material 4). Modes at this *PT* range correspond to plagioclase 45 wt%, cordierite 10 wt%, sillimanite 10 wt%, corundum 10 wt%, spinel 10 wt%, melt 15 wt%, ilmenite <1 wt%. Moreover, metastable andalusite grains account for an initial temperature below 650 °C, at a pressure that is further constrained by the absence of garnet to below 2 kbar. As a whole, the observations suggest an increase of temperature from *ca.* 650 °C to more than 900 °C, at a pressure lower than 2 kbar. This evolution is fully consistent with the evolution estimated for sample *Ma6*. Cooling may then have produced both crystallization of feldspar from the melt and possibly sillimanite fibers growing on andalusite crystals (Supplemental material 4).

7.5. *Ma5* xenolith

A pseudosection (Fig. 14) has been drawn for the local composition of a microdomain in sample *Ma5* (Fig. 4f and l). It differs from the sample at the sample scale in that there is no garnet relict. In the pseudosection, the mineral assemblage (cordierite + plagioclase + spinel + corundum + ilmenite ± biotite) is stable for temperature of higher than 800 °C and for pressure lower than 5 kbar. Mineral modes at 850 °C correspond to plagioclase 55 wt%, cordierite 9 wt%, spinel 10 wt%, ilmenite 2 wt%, K-feldspar 7 wt%, corundum 1 wt% and melt 16 wt%. These proportions are in close agreement with petrographic observations. The petrographic observation of spinel corona surrounding corroded corundum (Fig. 3k) argues for an increase of spinel proportions along with decrease of corundum above a temperature of 800 °C (Supplemental material 5). Although not visible in the microdomain, the presence of garnet relics elsewhere in the xenolith records previous

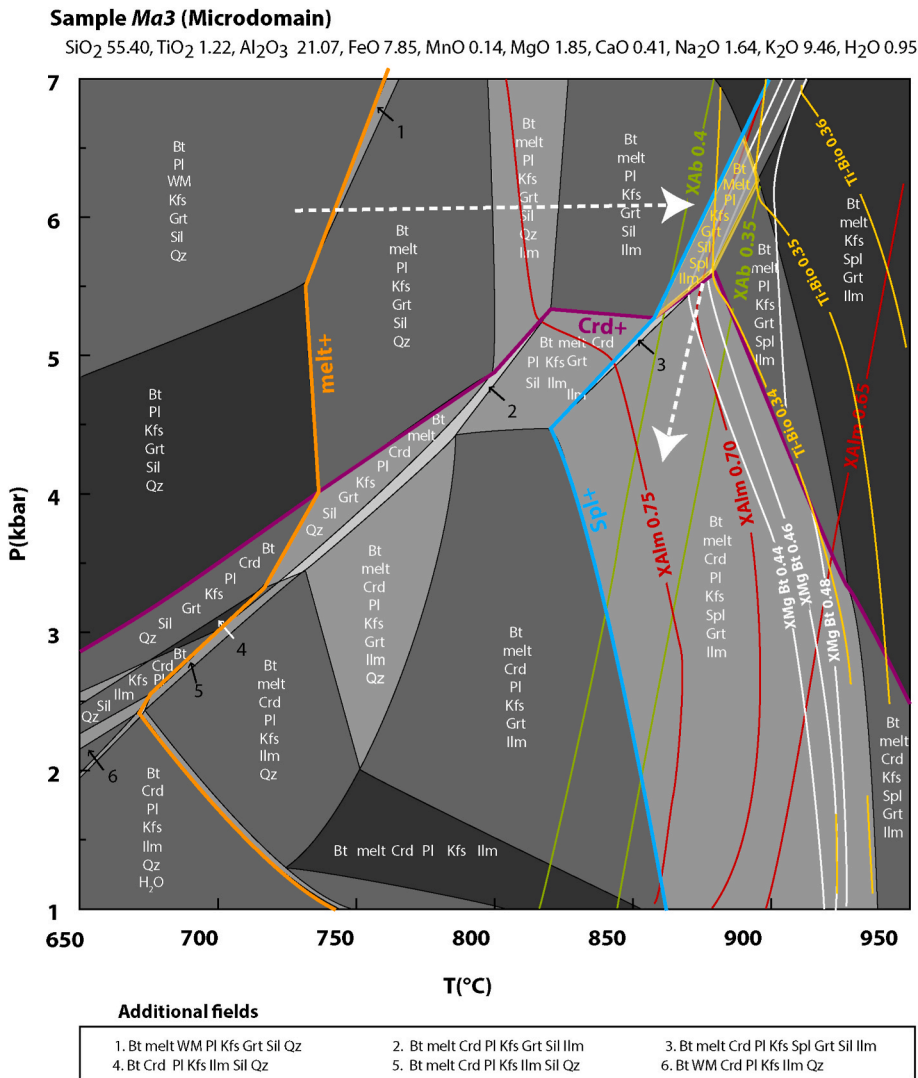


Fig. 10. Pressure-temperature pseudosection for sample Ma3. Composition in weight percent from EDS mapping of the microdomain shown in Fig. 4g. Also shown are the relevant isopleths for plagioclase (X_{Ab}), garnet (X_{Alm}) and biotite (X_{Mg} , Ti-Bio pfu) corresponding to the observed compositions (Tables 2 and 4), and the upper stability of cordierite. Pressure-temperature field corresponding to the paragenesis observed in the microdomain is underlined in yellow. The suggested prograde and retrograde paths are indicated by white dashed arrows. Mineral abbreviations from Whitney and Evans (2010).

mineral equilibrium at lower temperature and/or higher pressure (650–800 °C for pressures in the range 2.5–5 kbar).

8. Ages constraints

A few small (<10 μm) monazite crystals have been found in xenoliths Ma3 and Ma6. These were too small and rare for LA-ICPMS analyses but U–Pb dating was attempted by the U–Th–Pb chemical dating method by EPMA. The diameter of the interaction volume below the electron beam (4 μm) allowed only 7 analysis to be done in sample Ma6 and 21 in sample Ma3. In sample Ma6, individual data give ages lower than 230 Ma that do not define a single population. By contrast, in sample Ma3, the analyses, although slightly dispersed, provide an age of 293 ± 25 Ma, or, if restricted to a more coherent population of 11 analyses, 304 ± 3 Ma (Fig. 15).

9. A petrogenetic model for the crustal xenoliths from the Moroccan Central Massif

9.1. Evidence for prograde multi-stage evolution and partial melting in the xenoliths

Regional metamorphism is best represented in sample Ma3 where biotite, sillimanite and garnet underline the foliation and indicate pressure above ca. 5 kbar. In low pressure xenoliths (Ma6 and Kar2b),

euhedral crystals of andalusite, randomly scattered in the matrix, belong to an early paragenesis and may have formed during contact metamorphism prior to the entrapment or at the onset of heating in the dyke.

The peak temperature parageneses formed during ongoing partial melting, as shown by i) textural observations, i.e. the presence of feldspar-rich veinlets (e.g. Fig. 4c) and magmatic textures of feldspar associations (Fig. 3b, g and j), ii) chemical zoning of feldspar which witnesses fractional growth from a liquid (Fig. 4g, k), iii) the presence of ternary feldspar (Fig. 5a) that suggest that they formed under partial melting conditions at ca. 900 °C (Elkins and Grove, 1990).

In high pressure samples (Ma3, Ma10, Ma5), post-kinematic mineral associations formed during partial melting overprint foliated domains. These include coronas of cordierite + ilmenite + alkali feldspar around garnet (Figs. 3e and 4b and h) and spinel crystals crosscutting initial foliation (Fig. 3b) or as coronas around andalusite pseudomorphs (Fig. 3i). In low-pressure samples, secondary minerals associated to partial melting include coronas of spinel and plagioclase around and inside andalusite (Figs. 3f and 4e and k), and secondary sillimanite developed upon porphyroblasts of andalusite (Fig. 3e). The new products (including melt, neoblasts of spinel, cordierite, K-feldspar, ilmenite) formed from the (garnet) - biotite - andalusite (sillimanite) assemblages. (Cesare, 2000; Álvarez-Valero et al., 2007; Álvarez-Valero and Waters, 2010).

Partial melting reactions relevant to the conditions observed in the xenoliths of the Moroccan Central Massif have been reproduced in

Sample Ma10 (Whole-rock)

SiO₂ 46.20; TiO₂ 2.08; Al₂O₃ 35.47; FeO 6.50; MnO 0.13; MgO 1.81; CaO 0.70; Na₂O 2.03; K₂O 4.52; H₂O 0.54

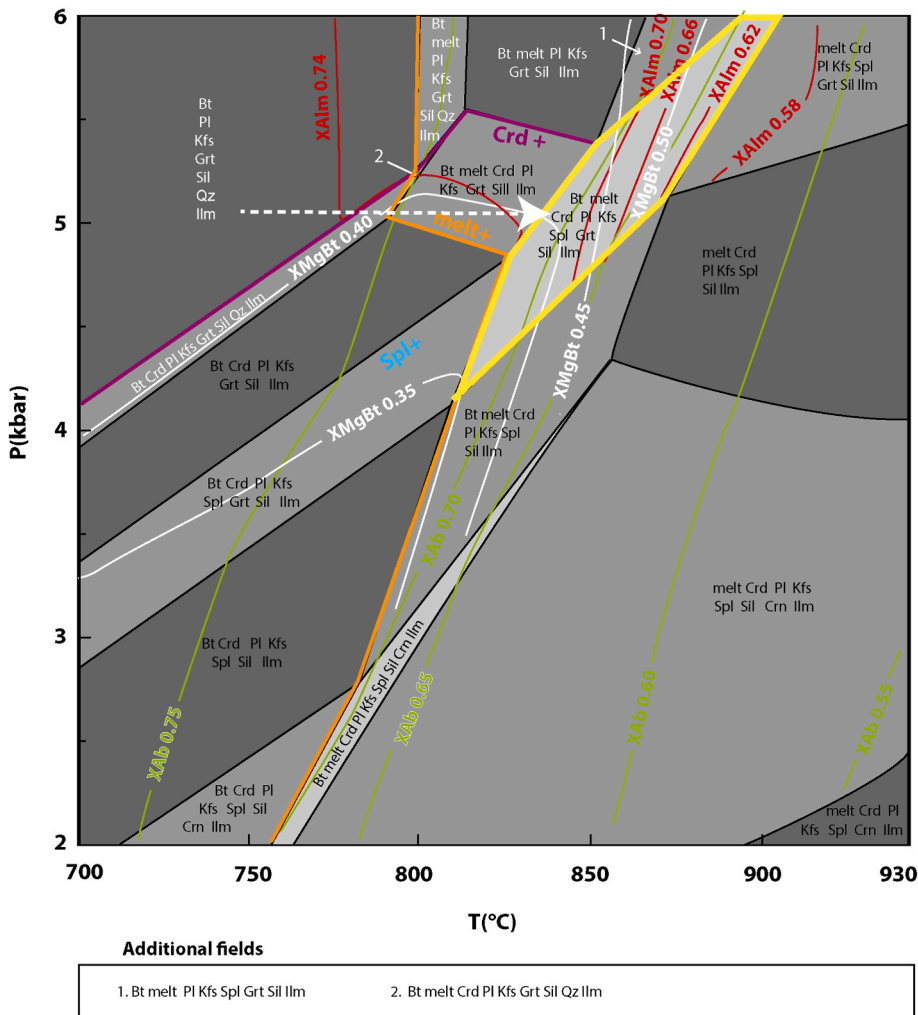
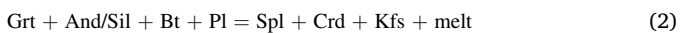
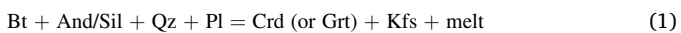
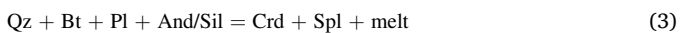


Fig. 11. Pressure-temperature pseudosection for sample *Ma10*. Composition in weight percent from whole-rock composition (Table 5). Also shown are the relevant isopleths for plagioclase (X_{Ab}), garnet (X_{Alm} , X_{Grs} , X_{Prp}) and biotite (X_{Mg}^{Bt}) corresponding to the observed compositions (Tables 2 and 4), and the upper stability of cordierite. Pressure-temperature field corresponding to the paragenesis observed in the microdomain is underlined in yellow. The suggested prograde path is indicated by a white dashed arrow. Mineral abbreviations from Whitney and Evans (2010).

experiments designed to reproduce assimilation of metasedimentary xenoliths in a granodioritic magma at lower crustal level (4 kbar) under water undersaturated conditions by Díaz-Alvarado et al. (2011). During heating and partial melting, they have shown that the initial parageneses of metapelitic xenoliths have evolved to form cordierite, spinel and K-feldspar. These minerals may be formed according to the well-studied reactions (e.g. Boulton et al., 1991; Vielzeuf and Holloway, 1988; Patiño Douce and Johnson, 1991; Johnson et al., 2004; Álvarez-Valero et al., 2007):



or, in garnet-free samples (Buick et al., 2004):



Experiments undertaken at 3 kbar from 700° to 1000 °C on water-rich or water-poor metapelites in order to explain contact metamorphism assemblages (Buick et al., 2004) also display mineral assemblages and melting reactions relevant to the present study. In water poor samples, partial melting begins slightly below 750 °C while muscovite, quartz, andalusite, biotite and plagioclase remain from the protolith and sillimanite appears as well as new crystals of cordierite, biotite and plagioclase. Spinel appears in the experiments at ca. 800 °C

and orthopyroxene at 1000 °C. Melt production is progressive with a main production between 800 and 950 °C when melt fraction reaches ca. 50%. An association of spinel + secondary plagioclase surrounding relicts of andalusite is noteworthy above 800 °C. Moreover, this secondary plagioclase appears richer in An, and melt is peraluminous granitic in composition with normative corundum. This evolution can be compared to that of the more silica-rich sample *Ma3*, the others having different, silica-depleted compositions. In sample *Ma3*, the paragenesis (Bt, Grt, Crd, Pl, Kfs, Spl, Ilm and melt) is comparable to those observed in the experiments between 800 and 900 °C, whereas the comparison with the thermodynamic model (Fig. 10) allows to reduce this interval to 850–900 °C for a pressure of ca. 5 kbar.

The melting reactions can be deciphered by a comparison of textural observation and thermodynamic modeling. For the composition of the microdomain in *Ma3* (Fig. 10), at high pressure (6 kbar), melting begins at ca. 750 °C (Fig. 16a) and involves consumption of biotite, plagioclase, quartz and produces low amount of garnet (reaction 1). The appearance of spinel is linked to a second major melt-producing reaction at 900 °C involving the consumption of sillimanite and biotite and the production of ilmenite together with spinel. This leads to the observed mineral assemblage in sample *Ma3* if we except late cordierite that appears at the expanse of garnet during decompression and cooling. At lower pressure (2.5 kbar, Fig. 16b), thermodynamic modeling shows that melting reaction begins at lower temperature (ca. 680 °C) and produces cordierite instead of garnet. The appearance of spinel as a peritectic phase takes

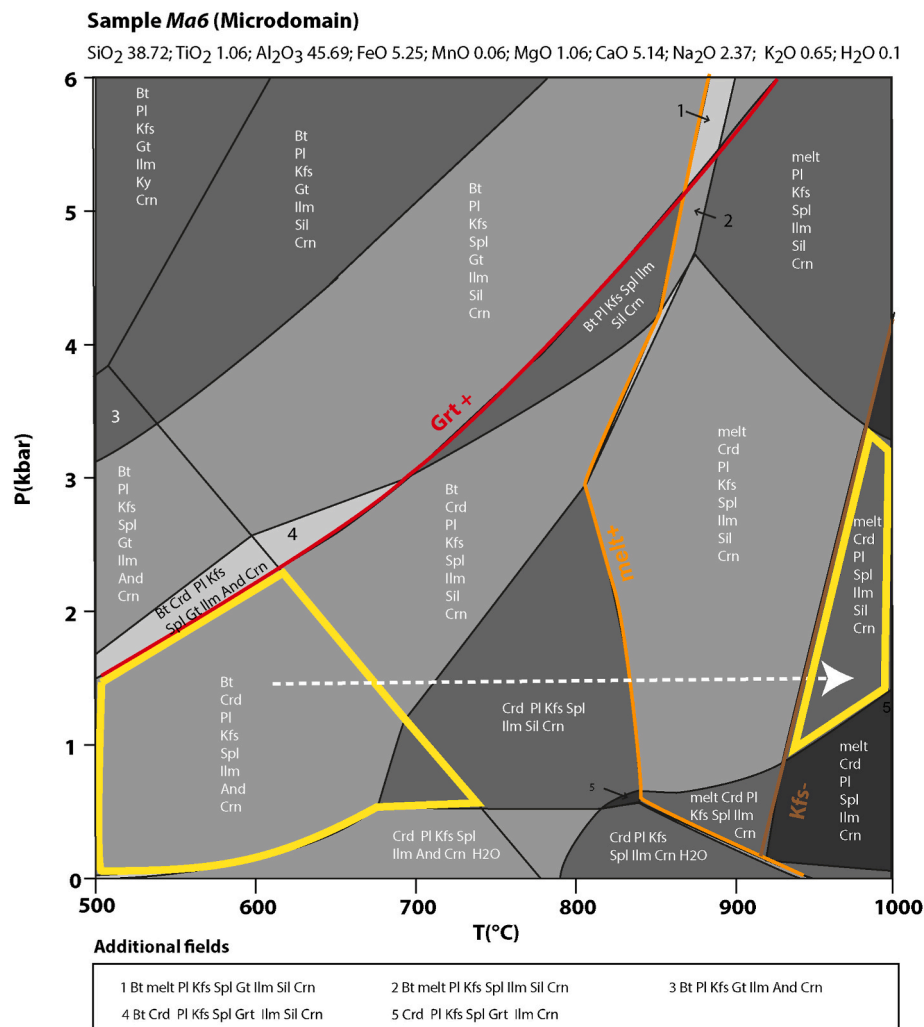


Fig. 12. Pressure-temperature pseudosection for sample *Ma6*. Composition in weight percent from EDS mapping of the microdomain shown in Fig. 4j. Also shown are the lower stability of garnet, the upper stability of K-feldspar and the solidus. Pressure-temperature field corresponding to the initial and final parageneses observed in the microdomain is underlined in yellow. Mineral abbreviations from Whitney and Evans (2010).

place at ca. 850 °C and melt is produced at the expense of biotite, plagioclase, K-feldspar and cordierite. Note also that partial melting leads to the disappearance of quartz at high temperature at 775–825 °C depending at low and high pressure respectively. However, for the composition of the microdomain in sample *Ma5* (Fig. 14), melting is slightly different (Fig. 16c). It is shifted to higher temperature (800 °C) and involves a single process of consumption of biotite, plagioclase and cordierite but also corundum and production of spinel, K-feldspar and ilmenite. According to the simulation, the growth of secondary cordierite in low temperature sample *Ma5* and *Kar2b* would not be directly related to partial melting but rather to an earlier solid-state reaction consuming biotite, sillimanite and small amounts of spinel to form cordierite, K-feldspar and corundum.

9.2. The significance of corundum and the depleted protolith of the xenoliths

Corundum has been observed in all samples except *Ma3*. These samples are characterized by their poor to intermediate SiO₂ and high Al₂O₃ content (44–57 wt% SiO₂, 17.5 wt% to 33.8 wt% Al₂O₃). Corundum belongs to the early mineral parageneses since it appears as inclusion in andalusite and garnets. However, it remains euhedral and stable in the late, high temperature parageneses together with feldspar and spinel. Thermodynamic calculations show that the presence of

corundum is controlled by the chemical composition rather than by the pressure-temperature conditions. Thus, in the simulations, corundum is absent when SiO₂ is higher than 50 wt% and Al₂O₃ lower than 30 wt% (Fig. 10), present over the whole PT range when SiO₂ is lower than 40 wt% and Al₂O₃ higher than 45 wt% (Figs. 12 and 13) and restricted to limited low-pressure domains (<5 kbar) at high temperature (>600 °C) for intermediate SiO₂ and Al₂O₃ contents (Figs. 11 and 14). Reaction textures preserved in spinel–corundum–feldspar-rich rocks show corundum partially replaced by spinel, which is consistent with numerical modelling that shows corundum consumption and spinel production above 800 °C (Fig. 16c) and has been already described by Johnson et al. (2010). It has been suggested that the presence of corundum is favoured by high H₂O content (Johnson et al., 2010). However, according to thermodynamic modelling corresponding to the composition of sample *Ma5* (Fig. 16d), an increase in H₂O content (from 0 to the observed value of 0.56 wt%) would rather correspond to the disappearance of corundum. At the composition corresponding to the studied microdomain, corundum is present at a pressure of 3 kb from 550 °C to 980 °C with a maximum modal abundance of 6% at ca. 850 °C.

9.3. Magma – xenoliths interactions and the origin of the refractory nature of the xenoliths

There are two lines of evidence for chemical – mechanical magma-

Sample Kar2b (Microdomain)

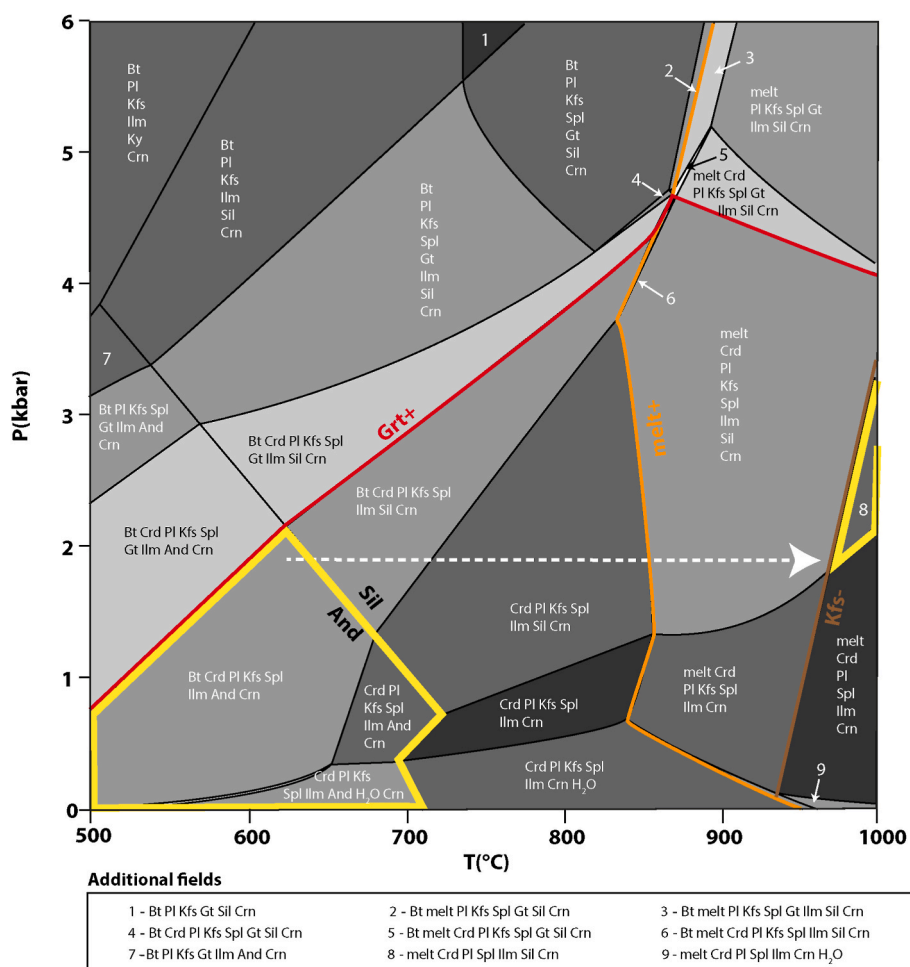
SiO₂ 35.76; TiO₂ 0.32; Al₂O₃ 49.11; FeO 6.46; MnO 0.07; MgO 1.75; CaO 3.17; Na₂O 1.71; K₂O 0.19; H₂O 0.14

Fig. 13. Pressure-temperature pseudosection for sample Kar2b. Composition in weight percent from EDS mapping of the microdomain shown in Fig. 4k. Also shown are the lower stability of garnet, the upper stability of K-feldspar and the solidus. Pressure-temperature field corresponding to the initial and final parageneses observed in the microdomain is underlined in yellow. Mineral abbreviations from Whitney and Evans (2010).

xenolith interactions in the samples from the Moroccan Central Massif. The first one is the petrographic observation of some digestion of the xenolith by the enclosing magma. This is marked by the presence of biotite and andalusite xenocrysts in the host rock at the contact with xenoliths in a number of samples (Fig. 3b, d and e). The second one is the observation of a linear relationship between the transition element and SiO₂ content in the host rock sampled in the vicinity of the xenoliths, which we tentatively interpret as a witness of chemical mixing between transition element enriched xenoliths and the enclosing magma (Fig. 8a). Such digestion of the xenoliths by the enclosing magma, and partial melting and melt loss due to heating at their contact, has been long observed and taken as a marker of crustal contamination during magma ascent. In particular, this process has been recently addressed on Díaz-Alvarado et al. (2011), which explained the shift from calc-alkaline magmas toward peraluminous granite composition by the assimilation of crustal xenolith that underwent partial melting and retained a solid fraction containing in particular the peritectic phases formed by partial melting reactions.

Such a process requires substantial amount of melt loss, which is difficult to evidence from the chemistry and the mineralogy of the residue. Indeed, as recalled by Johnson et al. (2010), melt loss at a given temperature would not change significantly mineral proportion and

chemical composition of the residue. Hence, the refractory nature of the xenolith, marked by the abundance of aluminosilicate phases, spinel and corundum, the low SiO₂ and large Al₂O₃ content, must be largely inherited from the protolith. Considering the partition coefficient from Bea et al., (1994) relevant for partial melting of crustal material, we have calculated the evolution of the trace element content of the residues for samples Ma3 (model 1) and Ma5 (model 2) in the case of non modal batch melting, i.e.

$$\frac{C_i}{C_0} = \frac{1}{D + F(1 - P)}$$

where C_i is the concentration of the element of interest in the partial melt, C_0 is the concentration in the initial solid, D is the bulk partition coefficient of the solid and P is the partition coefficient weighted by the proportion that each mineral contributes to the melt. Mineral proportion at the onset of cooling and the proportion of the mineral that contributes to the melt at a final temperature of 900 °C are taken from the thermodynamic calculation (Table 6). The two samples represent contrasted situation where, in the case of Ma3, melting is dominated by the consumption of biotite and quartz and garnet growth in the solid as a peritectic phase, while in the case of Ma5, cordierite and Kfs contribute significantly to melting in addition to biotite, in the absence of garnet. In

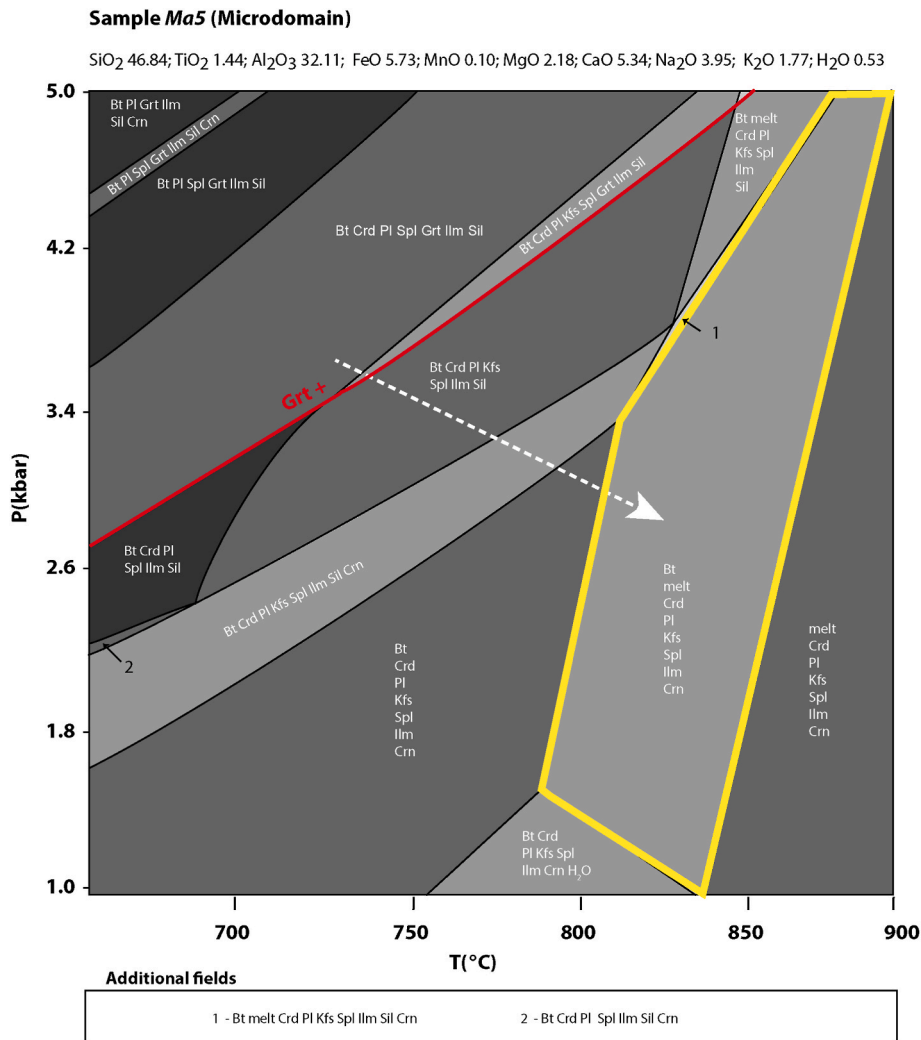


Fig. 14. Pressure-temperature pseudosection for sample *Ma5*. Composition in weight percent from EDS mapping of the microdomain shown in Fig. 41. Also shown is the lower stability of garnet. Pressure-temperature field corresponding to the assemblage observed in the microdomain is underlined in yellow. Mineral abbreviations from Whitney and Evans (2010).

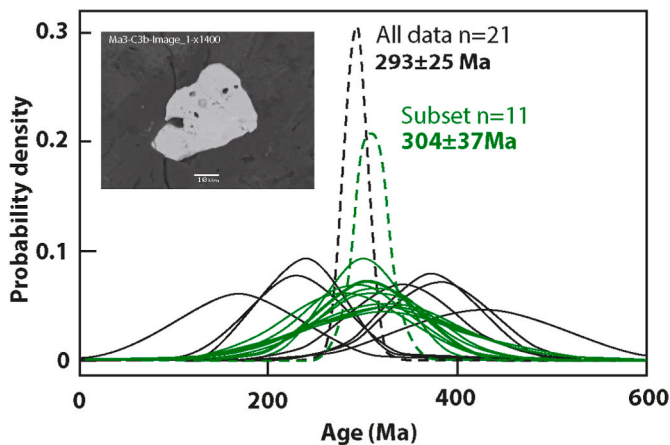


Fig. 15. U-Th-Pb chemical ages of monazite for sample *Ma3*.

the first case, the bulk partition coefficients for REE vary from 0.30 (Sm) to 12.17 (Lu) while in the second case, they vary from 0.89 (Sm) to 2.78 (La) (Table 6), i.e. in the first case, the LREE and MREE will behave as slightly incompatible elements whereas the HREE will behave as

compatible elements, whereas in the second case, all REE but Sm and Yb will behave as compatible elements during partial melting. In both cases, the bulk partition coefficients for transition elements are much higher than 1 and are generally higher in the case of *Ma3*. As a result, there will be very little variation in the trace element content of the residual solid C_s compared to the initial solid C_0 during partial melting at the considered temperature, where the melt fraction does not exceed 20%. The C_s/C_0 is in the range 0.7–1.23 and 0.96 to 1.1 respectively for REE for model 1 and model 2, and is in the range 1.14–1.23 and 1.05 to 1.15 for transition elements (Table 6). This is much lower than the observed variations among xenoliths (Fig. 9, Table 5), where the REE content varies by a factor of 4.5–7.5 depending on the REE and the transition element content by a factor of 2.1–2.9. Thus, the chemical diversity among xenolith cannot be attributed to different degrees of partial melting and melt extraction due to their incorporation in the magma. The diversity in major and trace element composition must be attributed to the diversity of their metapelitic protoliths. Thus, the protolith from which xenoliths have been derived must have undergone first partial melt extraction to explain their variable depletion in SiO₂ and enrichment in Al₂O₃ compared to standard metapelites. This must have taken place before entrapment in the magmas, i.e. during either earlier regional metamorphism or contact metamorphism related magma emplacement, as will be discussed below. This conclusion is in line with those proposed by other authors (e.g. Aguilar et al., 2016) that multiple

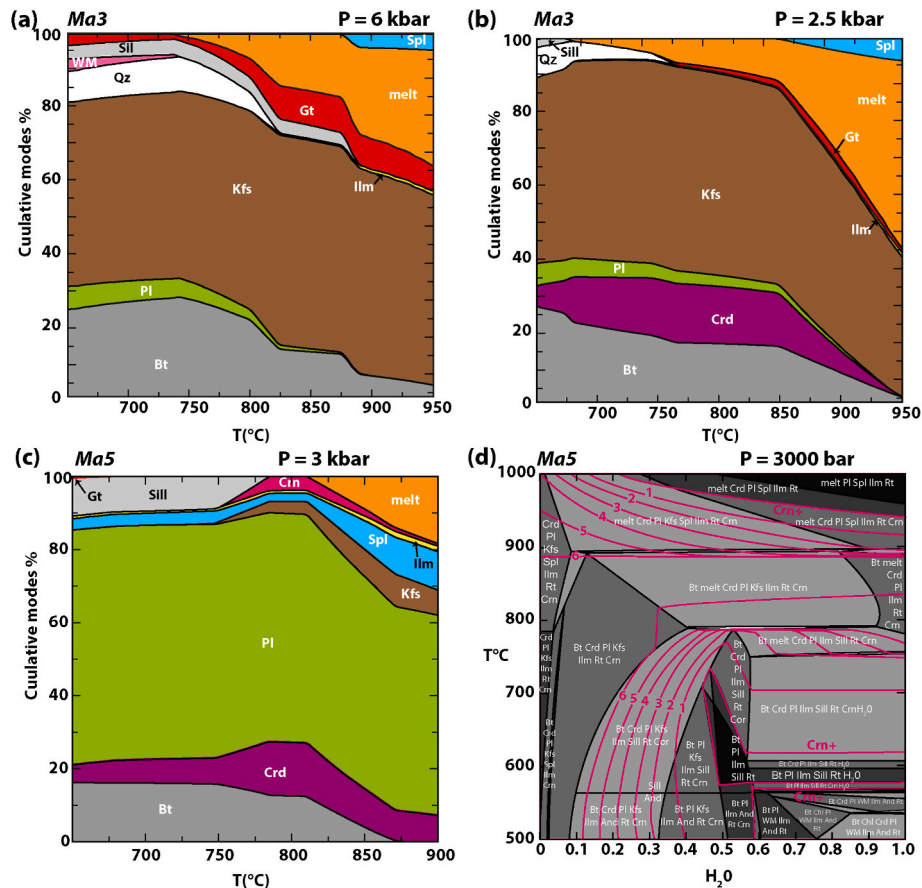


Fig. 16. Evolution of modal proportions of minerals from thermodynamic modeling. Cumulated modal proportion as a function of temperature for sample *Ma3* at 6 kbar (a) and 2.5 kbar (b) and for sample *Ma5* at 3 kbar (c). (d) Modal proportion of corundum as a function of T and $X(\text{H}_2\text{O})$ in sample *Ma5*, with $X = 1$ corresponding to 0.56 wt% H_2O .

melt extraction is necessary to shift the composition of the solid residue toward marked refractory composition.

10. Xenoliths as witnesses of metamorphic conditions of late Hercynian metamorphism in Moroccan Meseta

Three types of xenoliths can be distinguished based on their pressure-temperature record (Fig. 17). The first type, represented by samples *Ma3* and *Ma10*, record pressures higher than 5 kbar (as demonstrated by the presence of garnet) for temperatures exceeding 800 °C (as demonstrated by the presence of spinel associated to partial melting). A decompression path at high temperature is recorded in both samples by the transformation of garnet into cordierite. The second type, represented by sample *Ma5*, records intermediate pressure of ca 3 kbar for a temperature of 750–800 °C. Few garnet relics surrounded by a corona of cordierite testify for limited heating/decompression path. At last, samples *Ma6* and *Kar2b* exemplify a third type of xenoliths, that record low pressure (<2.5 kbar), as demonstrated by the abundance of andalusite relics and the absence of garnet. The transformation of an initial andalusite bearing assemblage into a sillimanite-cordierite-spinel-cordierite assemblage associated to partial melting records a major heating from below 700 °C to ca. 900 °C at constant pressure.

As a whole, the xenoliths have thus sampled a crustal segment from ca. 5–25 km (Fig. 17), considering a lithostatic pressure and a density of 2700 kg m⁻³. The overall pressure range recorded by the xenoliths matches the pressure range recorded by metamorphic rocks outcropping in the Rehamna (6–9 kbar; Aghzer et Arenas, 1998; Wernert et al., 2016), in the Jebilet (1.5–5 kbar; Delchini et al., 2016) and in the Eastern Meseta (6 kbar, Elabouyi et al., 2019) and by the crustal

xenoliths in late Hercynian magmas from the Jebilet (3 kbar, Bouloton et al., 1991), in the Middle Atlas (9–11 kbar; Moukadiri and Bouloton, 1998), and in the Zaër pluton (2–5 kbar, Haimeur et al., 2003). The absence of xenoliths recording a pressure higher than 11 kbar suggests either that the lower crustal levels have not been sampled by the magmas coming from the underlying mantle or that the Hercynian orogenic crust was only moderately thickened (less than 40 km) in the area.

Based on geochemical and isotopic data, it has been argued that the analogue Permian granodioritic magmas have a mixed mantle-crustal origin with limited crustal component (⁸⁷Sr/⁸⁶Sr up to 0.705; Mrini et al., 1992, for the Central Massif and the Rehamna; Gasquet et al., 1992 for the Tichka Massif; Youbi et al., 2001 and Dostal et al., 2005 for the dykes of the Jebilet). This is confirmed by the trace element data on the microgranodiorite and microgranite dykes from Kariane that show a marked negative Nb–Ta anomaly that can best be explained by crustal contamination in a late orogenic context.

The PT conditions recorded by the xenoliths corresponding to the maximum temperature are consistently in the range 800–900 °C, regardless of the pressure. Moreover, in xenoliths *Ma3* and *Ma10*, which record the highest pressure (ca. 6 kbar), the temperature associated to the earliest metamorphic stage (>850 °C) is higher than the metamorphic temperature at the same pressure reported from regional metamorphism associated to the orogenic stages in the D1–D2 deformation events in the Rehamna (Aghzer et Arenas, 1998; Wernert et al., 2016), in the Jebilet (Delchini et al., 2016) and in the Eastern Moulouya (Elabouyi et al. 2019) (Fig. 17). This suggests that the maximal temperature records thermal metamorphism associated to the incorporation into the magma, as already suggested by Bouloton (1991). The

Table 6
Non modal partial melting models.

	Model 1 Ma3			Model 2 Ma5		
Pressure <i>P</i> (kbar)	6			3		
Solidus temperature T_0 (°C)	738			810		
Peak temperature <i>T</i> (°C)	900			900		
Phase proportions (wt %)	at T_0	in the melting assemblage		at T_0	in the melting assemblage	
Bt	0.31	0.55		0.14	0.43	
Crd	0.00			0.14	0.21	
Pl	0.05	0.11		0.59	0.23	
Kfs	0.48			0.03		
Qz	0.10	0.23		0		
Sil	0.05	0.11		0		
Gt	0.02			0		
Sp	0.00			0.04		
Ilm	0.00			0.01		
Crn	0.00			0.06	0.13	
melt	0					
Final melt fraction (wt%)	21			15		
	<i>D</i> _{bulk}	<i>P</i>	<i>Cs/C₀</i>	<i>D</i> _{bulk}	<i>P</i>	<i>Cs/C₀</i>
La	0.72	0.54	0.94	2.78	1.08	1.11
Ce	0.61	0.46	0.90	2.34	0.91	1.10
Pr	0.64	0.51	0.91	2.55	1.01	1.11
Nd	0.40	0.33	0.78	1.55	0.63	1.07
Sm	0.30	0.19	0.71	0.89	0.38	1.00
Eu	1.27	0.36	1.07	1.85	0.70	1.08
Gd	0.52	0.28	0.88	1.29	0.57	1.05
Tb	1.26	0.42	1.07	1.92	0.94	1.08
Dy	2.11	0.31	1.14	1.33	0.72	1.05
Ho	3.69	0.29	1.18	1.34	0.82	1.05
Er	8.39	0.34	1.22	1.63	1.17	1.07
Tm	9.91	0.30	1.23	1.43	1.07	1.05
Yb	7.69	0.16	1.22	0.76	0.61	0.96
Lu	12.17	0.26	1.23	1.44	1.32	1.05
V	24.64	44.08	1.23	11.05	34.25	1.15
Cr	13.74	23.59	1.22	6.17	18.45	1.13
Ni	3.23	5.59	1.14	1.98	5.02	1.05
Nb	7.82	13.91	1.20	3.41	10.55	1.09

peak-temperature range (800–900 °C) recorded by the xenoliths lies in between the solidus (700–800 °C) and liquidus (900–1000 °C) temperatures calculated for the host magmas (Table 5) over the pressure range of 1–6 kbar with MELTS-Excel sheet (Gualda and Ghiorso, 2015). Given the small size of the xenoliths (<10 cm), thermal equilibrium between the host magma and the xenolith should be achieved in less than one day. On the other hand, the persistence of andalusite in a metastable form suggests a short metamorphic history. This is consistent with the characteristic cooling time *t* of ca. 10 days that can be estimated for a dyke of half-thickness *d* of 1 m considering a thermal diffusivity *K* of ca. $1 \times 10^{-6} \text{ m}^2 \text{ s}^{-1}$ and a conductive model where $t = d^2/(4K)$ (Turcotte and Schubert, 2003). The pressures and temperatures recorded by the xenoliths in Kariane are in good agreement with those reported in xenoliths in other places in Morocco (Fig. 17). The xenoliths in Oulad Ouaslam (Jebilet) described by Bouloton et al. (1991) record *PT* conditions of ca. 750 °C, 3 kbar, similar to xenolith Ma5. The xenoliths from the Zaër pluton (Central Massif) studied by Haïmeur et al. (2003) record *PT* conditions of 600–650 °C, 2–2.5 kbar for andalusite-bearing xenoliths, similar to xenoliths Ma6 and Kar2b, while corundum-spinel-bearing xenoliths record *PT* conditions of 690–770 °C, 4–5 kbar, similar to samples Ma3 and Ma10. The *PT* conditions retrieved from migmatitic terrains associated to both M-I type and S-type magmatism in the so-called Colline à Essaim d'Enclaves of the Eastern Meseta by Elabouyi et al. (2019) record an isobaric heating history with maximal *PT* condition in full agreement with those recorded by samples Ma3 and Ma10. At last, granulitic xenoliths from Plio-Quaternary basalts from the Middle Atlas record the highest pressures (9–11 kbar) for temperatures of ca. 900 °C similar to those of samples Kar2b and Ma6. In

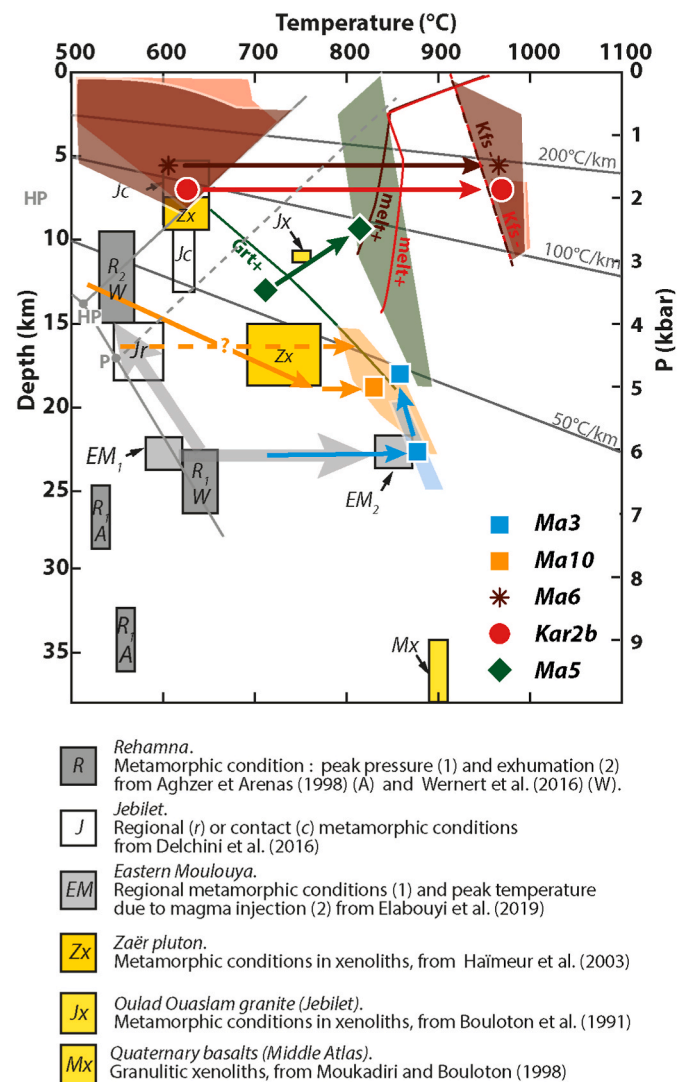


Fig. 17. Summary of pressure and temperature estimates for xenoliths of the Kariane locality. Pressure and temperature conditions for amphibolite to granulite facies Variscan metamorphism in Morocco estimated from previous work in regional metamorphism, contact metamorphism and in xenoliths from other localities are also shown. Position of the triple point for Al_2SiO_5 according to (HP) Holland and Powell (1998) or (P) Pattison (1992).

the case of the xenoliths from the Kariane locality, the age of the magmatic event responsible for the entrapment of the xenoliths in the dykes and the associated metamorphism is not well constrained. It can be attributed to the Permian both on stratigraphic grounds and on previous radiometric dating (Cheilletz, 1984; Rossi et al., 2016). The ages obtained in the present study on monazites from the xenolith (EPMA age of 293 ± 25 Ma) are consistent with those earlier age estimates.

The retrieval of the *PT* conditions that prevailed before the incorporation of the xenolith into the magma is difficult to assess. Regional metamorphism or syn-tectonic contact metamorphism is attested in the xenoliths from the Kariane locality by the oriented sillimanite-biotite-garnet association in sample Ma3, but the pressure-temperature record is obliterated by the temperature increase due to the entrapment in the magma. The early andalusite-bearing paragenesis in samples Ma6 and Kar2b records pressures and temperature conditions of ca. 600 °C for a pressure lower than 2.5 kbar, which is consistent both with the *PT* estimates of some of the xenoliths from the Zaër Pluton (Haïmeur et al., 2003) and with the temperature and pressure associated to contact

metamorphism in amphibolite facies in metapelites from the Jebilet Massif by Delchini et al. (2016). However, in sample *Ma10*, the presence of andalusite-chiastolite attesting for an early contact metamorphism implies *a priori* a pressure lower than 4 kbar, which is not consistent with the peak *PT* conditions (>4.5 kbar). This discrepancy may be explained either by a burial of the sample after contact metamorphism and before entrapment in the magma (orange line in Fig. 17), or if we admit a high-pressure high-temperature position for the silicate triple point (4.5 ± 0.5 kbar, 550 ± 35 °C) (Pattison, 1992; Cesare et al., 2003) rather than the position of the triple point from Holland and Powell (1998) data base used in the thermodynamic models (Fig. 17). In the latter case, slightly higher *P* and *T* conditions for the early andalusite-bearing stages are retrieved both for samples *Ma6* and *Kar2b* (ca. 700 °C for a pressure lower than 2.5 kbar) and the prograde evolution of sample *Ma10* can be explained by isobaric heating from 550 °C toward 800 °C at ca. 4.5 kbar (dashed orange line in Fig. 17). There is no available dating of those initial stages of metamorphism, which can represent either the early stage of heating and incorporation in the Permian dykes, or a former stage of contact metamorphism of the metasedimentary protoliths due to the intrusion of Carboniferous to Permian granitoids, such as described in the Jebilet, in the Rehamna, or in the neighbouring granitoid of Ment (e.g. Dahmani, 1995; Chopin et al., 2014; Delchini et al., 2016). Both regional metamorphism of the protolith and a pre-entrapment contact metamorphism and could have promoted early partial melting and melt extraction from the metasedimentary protolith and explain their refractory nature.

11. Conclusion

A suite of metapelitic xenoliths enclosed in a micro-quartz diorite dyke from the Moroccan Central Massif records granulite facies metamorphism, with maximal temperatures of 800 °C–900 °C. Peak pressure conditions varying from ca. 1.5–6 kbar depending on the xenolith. Stratigraphic constrains assign a Permian age for the micro-quartz diorite dyke, whereas U–Th/Pb EPMA dating on monazite in the xenoliths gives a date of 293 ± 25 Ma which, although poorly defined, confirms a late Variscan age for this metamorphism. The xenoliths therefore sample the first 25 km of the Variscan crust. However, the recorded maximal temperatures are systematically higher than the temperatures of the regional metamorphism associated to the Variscan tectono-metamorphic history. It is therefore concluded that the high temperature recorded in the xenoliths results from heating by the hot granodioritic host magmas.

The chemistry of the metapelitic xenoliths is generally silica-poor, aluminum-rich, which results in peculiar metamorphic quartz-absent assemblages comprising aluminosilicate (andalusite \pm sillimanite), corundum, spinel, cordierite and sometimes garnet. Although partial melt may have escaped the xenolith during entrapment in the magma, it is shown that melt loss cannot explain the refractory conditions observed in the xenoliths. The protoliths must therefore have been preconditioned by regional metamorphism or previous contact metamorphism at high temperature condition by a first depletion due to partial melting and melt loss. The remnants of this initial metamorphic stage can be found in the presence of andalusite, biotite and garnet crystals in some xenoliths.

Declaration of competing interest

The authors declare that they have no known competing financial interests or personal relationships that could have appeared to influence the work reported in this paper.

Acknowledgements

This project has been funded by CNRS–INSU–SYSTER program, by the University of Toulouse through an international partnership with

University Sidi Mohamed Ben Abdellah in Fez, Morocco. We are grateful to the head and members of the departement of geology of the University Sidi Mohamed Ben Abdellah of Fès for their support and welcome during meetings and field work. Many thanks to Antonio Álvarez-Valero, Ingrid van Namen and Joost van Hoeflaken who participated to this early field work and sampling in Morocco. This publication has been improved by the careful and constructive reviews of Bernardo Cesare and an anonymous reviewer.

Appendix A. Supplementary data

Supplementary data to this article can be found online at <https://doi.org/10.1016/j.jafrearsci.2022.104636>.

References

- Accotto, C., Martínez Poyatos, D., Azor, A., Jabaloy-Sánchez, A., Talavera, C., Evans, N. J., Azdimousa, A., 2020. Tectonic evolution of the eastern Moroccan Meseta: from late Devonian Forearc Sedimentation to early carboniferous collision of an Avalonian promontory. *Tectonics* 39, e2019TC005976.
- Acosta-Vigil, A., Buick, I.S., Hermann, J., Cesare, B., Rubatto, D., London, D., Morgan, G. B., 2010. Mechanisms of crustal anatexis: a geochemical study of partially melted metapelitic enclaves and host Dacite, SE Spain. *J. Petrol.* 51, 785–821.
- Aghzer, A.M., Arenas, R., 1995. Détachements et tectonique extensive dans le massif hercynien des Rehamna (Maroc). *J. Afr. Earth Sci.* 21, 383–393.
- Aghzer, A.M., Arenas, R., 1998. Evolution métamorphique des métapelites du Massif hercynien des Rehamna (Maroc): implications tectono-thermales. *J. Afr. Earth Sci.* 27, 87–106.
- Aguilar, C., Liesa, M., Reche, Powell, R., 2016. Fluid-fluxed melting and melt loss in a syntectonic contact metamorphic aureole from the Variscan eastern Pyrenees. *J. Metamorph. Geol.* 34, 379–400.
- Álvarez-Valero, A.M., Kriegsman, L.M., 2007. Crustal thinning and mafic underplating beneath the Neogene Volcanic Province (Betic Cordillera, SE Spain): evidence from crustal xenoliths. *Terra. Nova* 19, 266–271.
- Álvarez-Valero, A.M., Cesare, B., Kriegsman, L.M., 2007. Formation of spinel-cordierite-feldspar-glass coronas after garnet in metapelitic xenoliths: reaction modelling and geodynamic implications. *J. Metamorph. Geol.* 25, 305–320.
- Álvarez-Valero, A.M., Waters, D.J., 2010. Partially melted crustal xenoliths as a window into Sub-volcanic processes: evidence from the Neogene magmatic province of the Betic Cordillera, SE Spain. *J. Petrol.* 51, 973–991.
- Álvarez-Valero, A.M., Pla, F., Kriegsman, L.M., Geyer, A., Herrero, H., 2015. Observing silicic magma transport in dykes at depths of 8–19km: evidences from crustal xenoliths and numerical modelling. *J. Volcanol. Geoth. Res.* 296, 69–79.
- Bea, F., Pereira, M.D., Stroh, A., 1994. Mineral/leucosome trace-element partitioning in a peraluminous migmatite (a laser ablation-ICP-MS study). *Chem. Geol.* 117, 291–312.
- Ben Abbou, M., Soula, J.-C., Brusset, S., Roddaz, M., Ntarmouchant, A., Driouch, A., Christophoul, F., Bouadbelli, M., Majesté-Menjoules, C., Béziat, D., Debat, P., Déramond, J., 2001. Contrôle tectonique de la sédimentation dans le système de bassins d'avant-pays de la Meseta marocaine. *Comptes Rendus Acad. Sci. - Ser. IIA Earth Planet. Sci.* 332, 703–709.
- Berman, R.G., Aranovitch, L.Y., 1996. Optimized standard state and solution properties of minerals. I. Model calibration for olivine, orthopyroxene, cordierite, garnet, and ilmenite in the system FeO-MgO-CaO-Al₂O₃-SiO₂-TiO₂-H₂O-CO₂. *Contrib. Mineral. Petrol.* 126, 1–24.
- Boushaba, A., Cailleux, Y., 1992. Les relations métamorphisme-déformation au voisinage des granitoïdes hercynien du Maroc central. *Bull. Inst. Sci., Rabat* 16, 15–22.
- Bouloton, J., El Amrani, I., El Mourouah, A., et Montel, J.M., 1991. Les xénolithes hyperalumineux des granites, d'après l'exemple du pluton superficiel des Oulad Ouslam (Jbilet, Maroc). *C. R. Acad. Sci. Paris* 231, 273–279.
- Bouloton, J., Gasquet, D., 1995. Melting and undercooled crystallisation of felsic xenoliths from minor intrusions (Jebilet massif, Morocco). *Lithos* 35, 201–219.
- Buick, I.S., Stevens, G., Gibson, R.L., 2004. The role of water retention in the anatexis of metapelites in the Bushveld Complex Aureole, South Africa: an experimental study. *J. Petrol.* 45, 1777–1797.
- Carignan, J., Hild, P., Mevelle, G., Morel, J., Yeghicheyan, D., 2001. Routine Analyses of Trace Elements in Geological Samples Using Flow Injection and Low Pressure On-Line Liquid Chromatography Coupled to ICP-MS: A Study of Geochemical Reference Materials BR, DR-N, UB-N, AN-G and GH. *Geostandards Newsletter*, 25, pp. 187–198.
- Cesare, B., 2000. Incongruent melting of biotite to spinel in a quartz-free restite at El Joyazo (SE Spain): textures and reaction characterization. *Contrib. Mineral. Petrol.* 139, 273–284.
- Cesare, B., Marchesi, C., Hermann, J., Gómez-Pugnaire, M.T., 2003. Primary melt inclusions in andalusite from anatectic graphitic metapelites: implications for the position of the Al₂SiO₅ triple point. *Geology* 31, 573–576.
- Cheilletz, A., 1984. Contribution à la géologie du district polymétallique (W, Mo, Cu, Zn, Ag) du Djebel Aouam (Maroc Central, application à la prospection des gisements de tungstène). Thèse de doctorat ès-Sciences, I.P.T.L. Nancy, p. 250.
- Chopin, F., Corsini, M., Schulmann, K., El Houicha, M., Ghiene, J.-F., Edel, J.-B., 2014. Tectonic evolution of the Rehamna metamorphic dome (Morocco) in the context of the Alleghanian-Variscan orogeny. *Tectonics* 33, 1154–1177.

- Coggon, R., Holland, T.J.B., 2002. Mixing properties of phengitic micas and revised garnet-phengite thermobarometers. *J. Metamorph. Geol.* 20, 683–696.
- Connolly, J.A.D., 2005. Computation of phase equilibria by linear programming: a tool for geodynamic modeling and its application to subduction zone decarbonation. *Earth Planet. Sci. Lett.* 236, 524–541.
- Connolly, J.A.D., 2009. The geodynamic equation of state: what and how. *G-cubed* 10, Q10014.
- Corsini, M., Rolland, Y., 2009. Late evolution of the southern European Variscan belt: exhumation of the lower crust in a context of oblique convergence. *Compt. Rendus Geosci.* 341, 214–223.
- Cox, K.G., Bell, J.D., Pankhurst, R.J., 1979. *The Interpretation of Igneous Rocks*. George Allen & Unwin, London, p. 450.
- Dahmani, A., 1995. Développement des auroles de contact d'Oulmès et de Ment (Maroc Central): étude, zones métamorphiques et histoires de réchauffement et de refroidissement. Chicoutimi, PhD thesis. Université du Québec.
- Depine, G.V., Andronicos, C.L., Phipps-Morgan, J., 2008. Near-isothermal conditions in the middle and lower crust induced by melt migration. *Nature* 452, 80–83.
- Delchini, S., Lahfid, A., Lacroix, B., Baudin, T., Hoepffner, C., Guerrot, C., Lach, P., Saddiqi, O., Ramboz, C., 2018. The geological evolution of the variscan Jebilet massif, Morocco, inferred from new structural and geochronological analyses. *Tectonics* 37, 4470–4493.
- Delchini, S., Lahfid, A., Plunder, A., Michard, A., 2016. Applicability of the RSCM geothermometry approach in a complex tectono-metamorphic context: the Jebilet massif case study (Variscan Belt, Morocco). *Lithos* 256–257, 1–12.
- Díaz-Alvarado, J., Castro, A., Fernández, C., Moreno-Ventas, I., 2011. Assessing bulk assimilation in cordierite-bearing granitoids from the Central System Batholith, Spain; experimental, geochemical and geochronological constraints. *J. Petrol.* 52, 223–256.
- Dostal, J., Keppie, J.D., Hamilton, M.A., Aarab, E.M., Lefort, J.P., Murphy, J.B., 2005. Crustal xenoliths in Triassic lamprophyre dykes in western Morocco: tectonic implications for the Rheic Ocean suture. *Geol. Mag.* 142, 159–172.
- Duchene, S., Fornelli, A., Micheletti, A.-M., Piccarreta, G., 2013. Sm-Nd chronology of porphyroblastic garnets from granulite facies metabasic rocks in Calabria (Southern Italy): inferences for preserved isotopic memory and resetting. *Mineral. Petrol.* 107, 539–551.
- Elabouyi, M., Dahire, M., Driouch, Y., Duchêne, S., Kriegsman, L.M., Ntarmouchant, A., Kahou, Z.S., Severac, J.L., Belkassi, M., Debat, P., 2019. Crustal anatexis in the Aouli-Mibladen granitic complex: a window into the middle crust below the Moroccan Eastern Variscan Meseta. *J. Afr. Earth Sci.* 154, 136–163.
- Elkins, L.T., Grove, T.L., 1990. Ternary feldspar experiments and thermodynamic models. *Am. Mineral.* 75, 544–559.
- England, P.C., Thompson, A.B., 1984. Pressure-Temperature-time path of regional metamorphism: I Heat transfer during the evolution of regions of thickened metamorphic rocks. *J. Petrol.* 25, 894–928.
- Essaifi, A., Potrel, A., Capdevila, R., Lagarde, J.-L., 2003. U–Pb dating: emplacement age of the bimodal magmatism of central Jebilet (Variscan Belt, Morocco). *Geodynamic implications*. *Compt. Rendus Geosci.* 335, 193–203.
- Fornelli, A., Langone, A., Micheletti, A.-M., Piccarreta, G., 2011. Time and duration of Variscan high-temperature metamorphism processes in the south European Variscides: constraints from U–Pb chronology and trace element chemistry of zircon. *Mineral. Petrol.* 103, 101–122.
- Gasquet, D., Leterrier, J., Mrini, Z., Vidal, P., 1992. Petrogenesis of the hercynian Tichka plutonic complex (western high Atlas, Morocco): trace element and Rb–Sr and Sm–Nd isotopic constraints. *Earth Planet. Sci. Lett.* 108, 29–44.
- Gasquet, D., Bertrand, J.-M., Paquette, J.-L., Lehmann, J.R.M., Ratzov, G., De Ascensão Guedes, R., Tiepolo, M., Boullier, A.-M., Scailliet, S., Nomade, S., 2010. Miocene to Messinian deformation and hydrothermal activity in a pre-Alpine basement massif of the French western Alps: new U–Th–Pb and argon ages from the Lauzière massif. *Bull. Soc. Geol. Fr.* 181, 227–241.
- Gonçalves, G.O., Lana, C., Scholz, R., Buick, I.S., Gerdes, A., Kamo, S.L., Corfu, F., Marinho, M.M., Chaves, A.O., Valeriano, C., Nalini Jr., H.A., 2016. An assessment of monazite from the Itambe pegmatite district for use as U–Pb isotope reference material for microanalysis and implications for the origin of the "Moacyr" monazite. *Chem. Geol.* 424, 30–50.
- Graessner, T., Schenk, V., 2001. An exposed Hercynian deep crustal section in the Sila Massif of Northern Calabria: mineral chemistry, petrology, and P–T path of granulite-facies metapelitic migmatites and metabasites. *J. Petrol.* 42, 931–961.
- Gualda, G.A.R., Ghiorso, M.S., 2015. MELTS Excel: a Microsoft Excel-based MELTS interface for research and teaching of magma properties and evolution. *G-cubed* 16, 315–324.
- Guitard, G., Vielzeuf, D., Martinez, F., 1995. Synthèse Géologique et Géophysique des Pyrénées - Le Métamorphisme Hercynien. pp. 501–584.
- Haïmeur, J., Chabane, A., El Amrani El Hassani, I.-E., 2003. Analyse pétro-minéralogique des interactions granite-enclaves dans le pluton hercynien de Zaër (Maroc central) : implications pétrogénétiques. *Bulletin de l'Institut Scientifique, Rabat, section Sciences de la Terre* n°25, pp. 1–29.
- Hoepffner, C., Soulaïmani, A., Piqué, A., 2005. The Moroccan Hercynides. *J. Afr. Earth Sci.* 43, 144–165.
- Holland, T., Powell, R., 1998. An internally consistent thermodynamic data set for phases of petrological interest. *J. Metamorph. Geol.* 16, 309–343.
- Janoušek, V., Farrow, C.M., Erban, V., 2006. Interpretation of whole-rock geochemical data in igneous geochemistry: introducing Geochemical Data Toolkit (GCDKit). *J. Petrol.* 47, 1255–1259.
- Johnson, T., Brown, M., Gibson, R., Wing, B., 2004. Spinel cordierite symplectites replacing andalusite: evidence for melt assisted diapirism in the Bushveld Complex, South Africa. *J. Metamorph. Geol.* 22, 529–545.
- Johnson, T.E., Brown, M., White, R.W., 2010. Petrogenetic modelling of strongly residual metapelitic xenoliths within the southern Platreef, Bushveld Complex, South Africa. *J. Metamorph. Geol.* 28, 269–291.
- Johnson, T.E., White, R.W., Brown, M., 2011. A year in the life of an aluminous metapelite xenolith—the role of heating rates, reaction overstep, H₂O retention and melt loss. *Lithos* 124, 132–143.
- Juez-Larré, J., Ter Voorde, M., 2009. Thermal impact of the break-up of Pangea on the Iberian Peninsula, assessed by thermochronological dating and numerical modelling. *Tectonophysics* 474, 200–213.
- Kunz, B.E., Manzotti, P., von Niederhäusern, B., Engi, M., Darling, J.R., Giuntoli, F., Lanari, P., 2018. Permian high-temperature metamorphism in the western Alps (NW Italy). *Int. J. Earth Sci.* 107, 203–229.
- Lahfid, A., Baidder, L., Ouanaimi, H., Soulaïmani, A., Hoepffner, C., Farah, A., Saddiqi, O., Michard, A., 2019. From extension to compression: high geothermal gradient during the earliest Variscan phase of the Moroccan Meseta; a first structural and RSCM thermometric study. *Eur. J. Mineral.* 31, 695–713.
- Martínez Catalán, J.R., Schulmann, K., et al., 2021. The Mid-Variscan Allochthon: keys from correlation, partial retrodeformation and plate-tectonic reconstruction to unlock the geometry of a non-cylindrical belt. *Earth Sci. Rev.* 220, 103700.
- McDonough, W.F., Sun, S., 1995. The composition of the Earth. *Chem. Geol.* 120, 223–253.
- Michard, A., Hoepffner, C., Soulaïmani, A., Baidder, L., 2008. The variscan belt. In: Michard, A. (Ed.), *Continental Evolution: the Geology of Morocco*. Springer-Verlag, Berlin Heidelberg, pp. 65–132.
- Michard, A., Soulaïmani, A., Hoepffner, C., Ouanaimi, H., Baidder, L., Rjimati, E.C., Saddiqi, O., 2010. The south-western branch of the variscan belt: evidence from Morocco. *Tectonophysics* 492, 1–24.
- Montel, J.-M., Foret, S., Veschambre, M., Nicollet, C., Provost, A., 1996. Electron microprobe dating of monazite. *Chem. Geol.* 131, 37–53.
- Moukadi, A., Bouloton, J., 1998. Pétrologie des granulites exhumées par le volcanisme récent du Moyen Atlas : aperçu sur la croûte inférieure néogène du Maroc central. *Comptes Rendus Acad. Sci. - Ser. IIA Earth Planet. Sci.* 327, 731–734.
- Mrini, Z., Rafi, A., Duthou, J.L., Vidal, P., 1992. Chronologie Rb–Sr des granitoides hercyniens du Maroc; conséquences. *Bull. Soc. Geol. Fr.* 163, 281–291.
- Nakamura, N., 1974. Determination of REE, Ba, Fe, Mg, Na and K in carbonaceous and ordinary chondrites. *Geochem. Cosmochim. Acta* 38, 757–775.
- Newton, R.C., Charlu, T.V., Kleppa, O.J., 1980. Thermochemistry of the high structural state plagioclases. *Geochem. Cosmochim. Acta* 44, 933–941.
- Ntarmouchant, A., 2003. Le magmatisme associé aux bassins carbonifères d'avant-pays : Exemple du magmatisme bassin méridional d'Azrou-Khénifra (Est du Maroc Hercynien Central). *Nature métasédimentaire du sous-bassement, contexte de mise en place et implication géodynamique*. Thèse ès sciences. Université Sidi Mohammed Ben Abdellah, Fès, p. 312.
- Patiño Douce, A.E., Johnson, A.D., 1991. Phase equilibria and melt productivity in the pelitic system: implications for the origin of peraluminous granitoids and aluminous granulites. *Contrib. Mineral. Petrol.* 107, 2020–2218.
- Pattison, D.R.M., 1992. Stability of andalusite and sillimanite and the Al₂SiO₅ triple point: constraints from the Ballachulish aureole, Scotland. *J. Geol.* 100, 423–446.
- Petri, B., Mohn, G., Skrzypek, E., Mateeva, T., Galster, F., Manatschal, G., 2017. U–Pb geochronology of the Sondalo gabbroic complex (Central Alps) and its position within the Permian post-Variscan extension. *Int. J. Earth Sci.* 106, 2873–2893.
- Piqué, A., Michard, A., 1989. Moroccan Hercynides, a synopsis. The Palaeozoic sedimentary and tectonic evolution at the northern margin of West Africa. *Am. J. Sci.* 289, 286–330.
- Powell, R., Downes, J., 1990. Garnet porphyroblast-bearing leucosomes in metapelites: mechanisms, phase diagrams, and an example from Broken Hill, Australia. In: Ashworth, J.R., Brown, M. (Eds.), *High-Temperature Metamorphism and Crustal Anatexis*. Unwin, London, pp. 105–123.
- Roddaz, M., Brusset, S., Soula, J.-C., Béziat, D., Ben Abbou, M., Debat, P., Driouch, Y., Christophoul, F., Ntarmouchant, A., Déramond, J., 2002. Foreland basin magmatism in the Western Moroccan Meseta and geodynamic inferences. *Tectonics* 21, 7–17–23.
- Rossi, P., Cocherie, A., Fanning, C.M., 2015. Evidence in Variscan Corsica of a brief and voluminous Late Carboniferous to Early Permian volcanic-plutonic event contemporaneous with a high-temperature/low-pressure metamorphic peak in the lower crust. *Bull. Soc. Geol. Fr.* 186, 171–192.
- Rossi, M., Tarrieu, L., Cheilletz, A., Gasquet, D., Delouie, E., Paquette, J.-L., Bounajma, H., Mantoy, T., Ouazzani, L., Ouchtouban, L., 2016. The Polymetallic (W–Au and Pb–Zn–Ag) Tighza district (Central Morocco): ages of magmatic and hydrothermal events. In: Bouabdellah, M., Slack, J.F. (Eds.), *Mineral Deposits of North Africa*. Mineral Resource Reviews, pp. 107–131.
- Seydoux-Guillaume, A.M., Wirth, R., Nasdala, L., Gottschalk, M., Montel, J.M., Heinrich, W., 2002. An XRD, TEM and Raman study of experimentally annealed natural monazite. *Phys. Chem. Miner.* 29, 240–253.
- Seydoux-Guillaume, A.-M., Montel, J.-M., Bingen, B., Bosse, V., de Parseval, P., Paquette, J.-L., Janots, E., Wirth, R., 2012. Low-temperature alteration of monazite: fluid mediated coupled dissolution–precipitation, irradiation damage, and disturbance of the U–Pb and Th–Pb chronometers. *Chem. Geol.* 330–331, 140–158.
- Simancas, J.F., Tahiri, A., Azor, A., González-Lodeiro, F., Martínez-Poyatos, D., El Hadi, H., 2005. The tectonic frame of the variscan–Alleghean orogen in southern Europe and northern Africa. *Tectonophysics* 398, 181–198.
- Simancas, J.F., Azor, A., Martínez-Poyatos, D., Tahiri, A., El Hadi, H., González-Lodeiro, F., Pérez-Estaún, A., Carbonell, R., 2009. Tectonic relationships of Southwest Iberia with the allochthons of Northwest Iberia and the Moroccan Variscides. *Compt. Rendus Geosci.* 341, 103–113.

- Siron, G., Goncalves, P., Marquer, D., Pierre, T., Paquette, J.-L., Vanardois, J., 2020. Contribution of magmatism, partial melting buffering and localized crustal thinning on the late Variscan thermal structure of the Agly massif (French Pyrenees). *J. Metamorph. Geol.* 1–31.
- Stampfli, G.M., Borel, G.D., 2002. A plate tectonic model for the Paleozoic and Mesozoic constrained by dynamic plate boundaries and restored synthetic oceanic isochrons. *Earth Planet Sci. Lett.* 196, 17–33.
- Tajčmanová, L., Connolly, J.A.D., Cesare, B., 2009. A thermodynamic model for titanium and ferric iron solution in biotite. *J. Metamorph. Geol.* 27, 153–165.
- Turcotte, D.L., Schubert, L., 2003. *Geodynamics*. Cambridge University Press, p. 456.
- van Hoeflaken, J., 2011. Hercynian UHT Metamorphism of Crustal Xenoliths from Bou Ibaighatene and Tafraoute, Middle Atlas, Morocco. Unpublished MSc Thesis, Utrecht University.
- Vielzeuf, D., Holloway, J.R., 1988. Experimental determination of the fluid-absent melting relations in the pelitic system. *Contrib. Mineral. Petrol.* 98, 257–276.
- Villa-Vialaneix, N., Montel, J.-M., Seydoux-Guillaume, A.-M., 2013. NiLeDAM: Monazite Datation for the NiLeDAM Team. R package version 0.1.
- Waldbaum, D.R., Thompson, J.B., 1968. Mixing properties of sanidine crystalline solutions: II Calculations based on volume data. *Am. Mineral.* 53, 2000–2017.
- Wernert, P., Schulmann, K., Chopin, F., Štípská, P., Bosch, D., El Houicha, M., 2016. Tectonometamorphic evolution of an intracontinental orogeny inferred from P–T–d paths of the metapelites from the Rehamna massif (Morocco). *J. Metamorph. Geol.* 34, 917–940.
- White, R.W.P.R., Holland, J.B., Worley, B., 2000. The effect of TiO₂ and Fe₂O₃ on metapelitic assemblages at greenschist and amphibolite facies conditions: mineral equilibria calculations in the system K₂O-FeO-MgO-Al₂O₃-SiO₂-H₂O-TiO₂-Fe₂O₃. *J. Metamorph. Geol.* 18, 497–511.
- White, R.W., Powell, R., Holland, J.B., 2001. Calculation of partial melting equilibria in the system Na₂O-CaO-K₂O-FeO-MgO-Al₂O₃-SiO₂-H₂O (NCKFMASH). *J. Metamorph. Geol.* 19, 139–153.
- Whitney, D.L., Evans, B.W., 2010. Abbreviations for names of rock-forming minerals. *Am. Mineral.* 95, 185–187.
- Youbi, N., Bellon, H., Marzin, A., Piqué, A., Cotten, J., Cabanis, B., 2001. Du cycle orogénique hercynien au pré-rifting de l'Atlantique central au Maroc Occidental : les microdiorites des Jbilet sont-elles des marqueurs magmatiques de ce passage. *Comptes Rendus Acad. Sci. - Ser. IIA Earth Planet. Sci.* 333, 295–302.